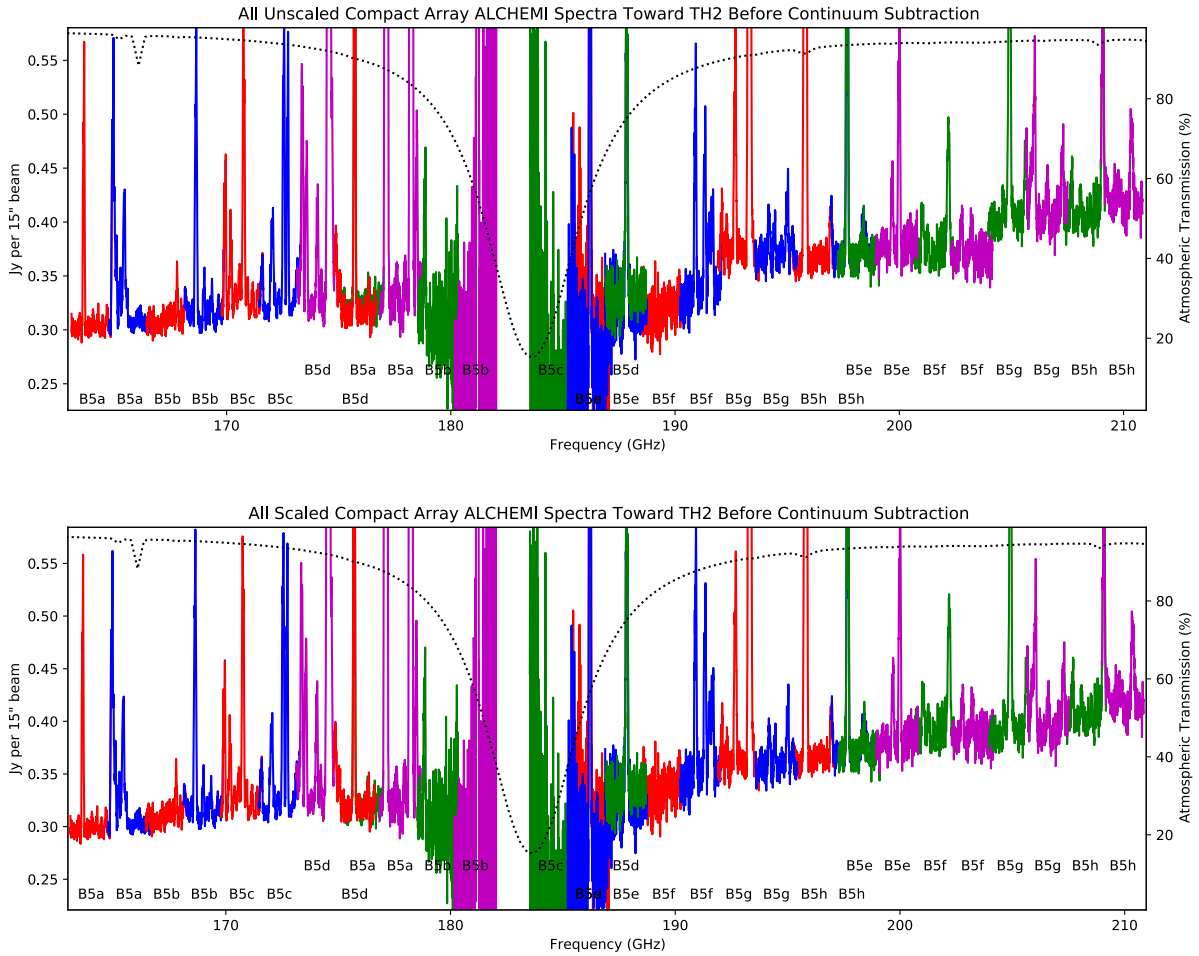

Fig. B.4. Same as Fig. B.2 but for Band 5 unscaled (top) and scaled (bottom).

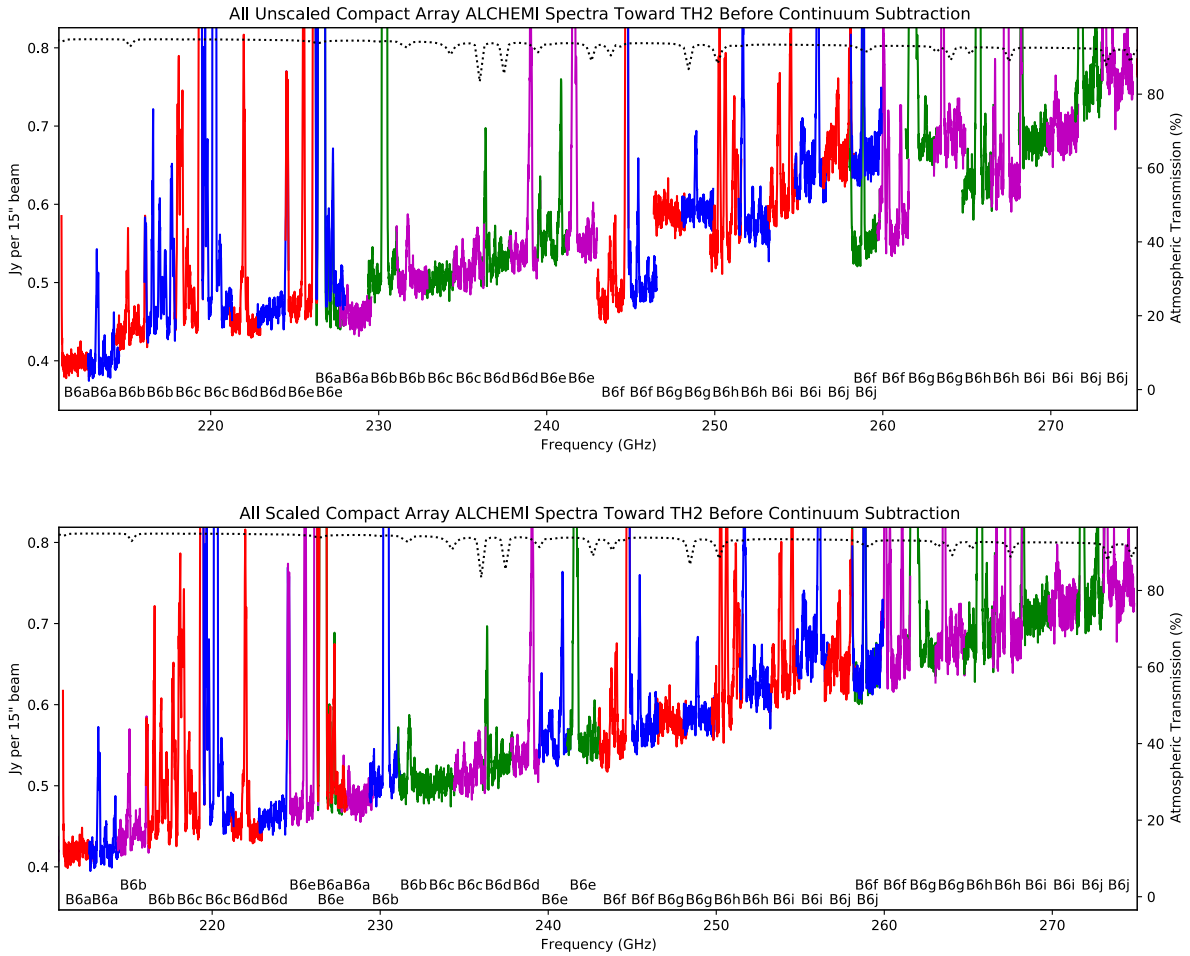

Fig. B.5. Same as Fig. B.2 but for Band 6 unscaled (top) and scaled (bottom).

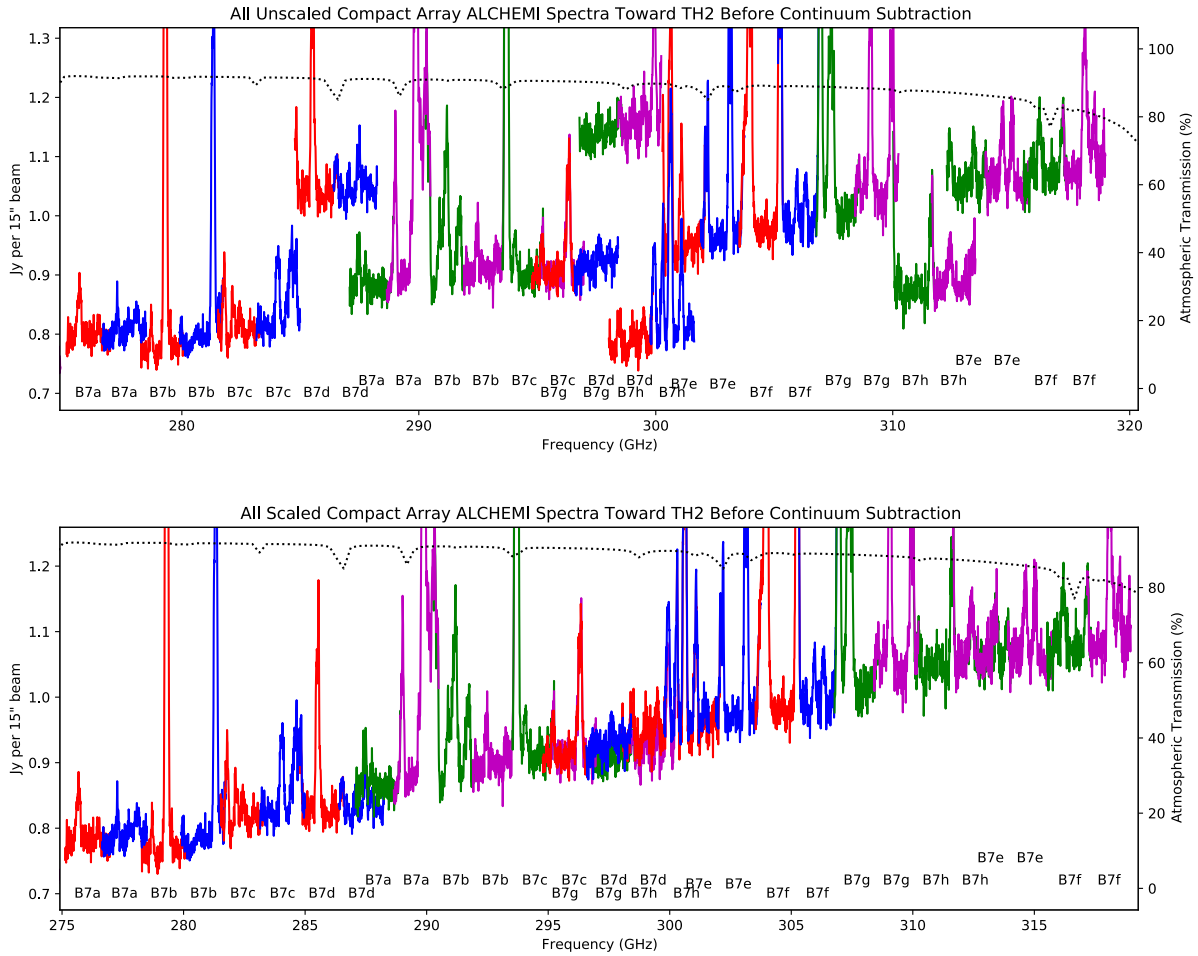

Fig. B.6. Same as Fig. B.2 but for the first-half of Band 7 unscaled (top) and scaled (bottom).

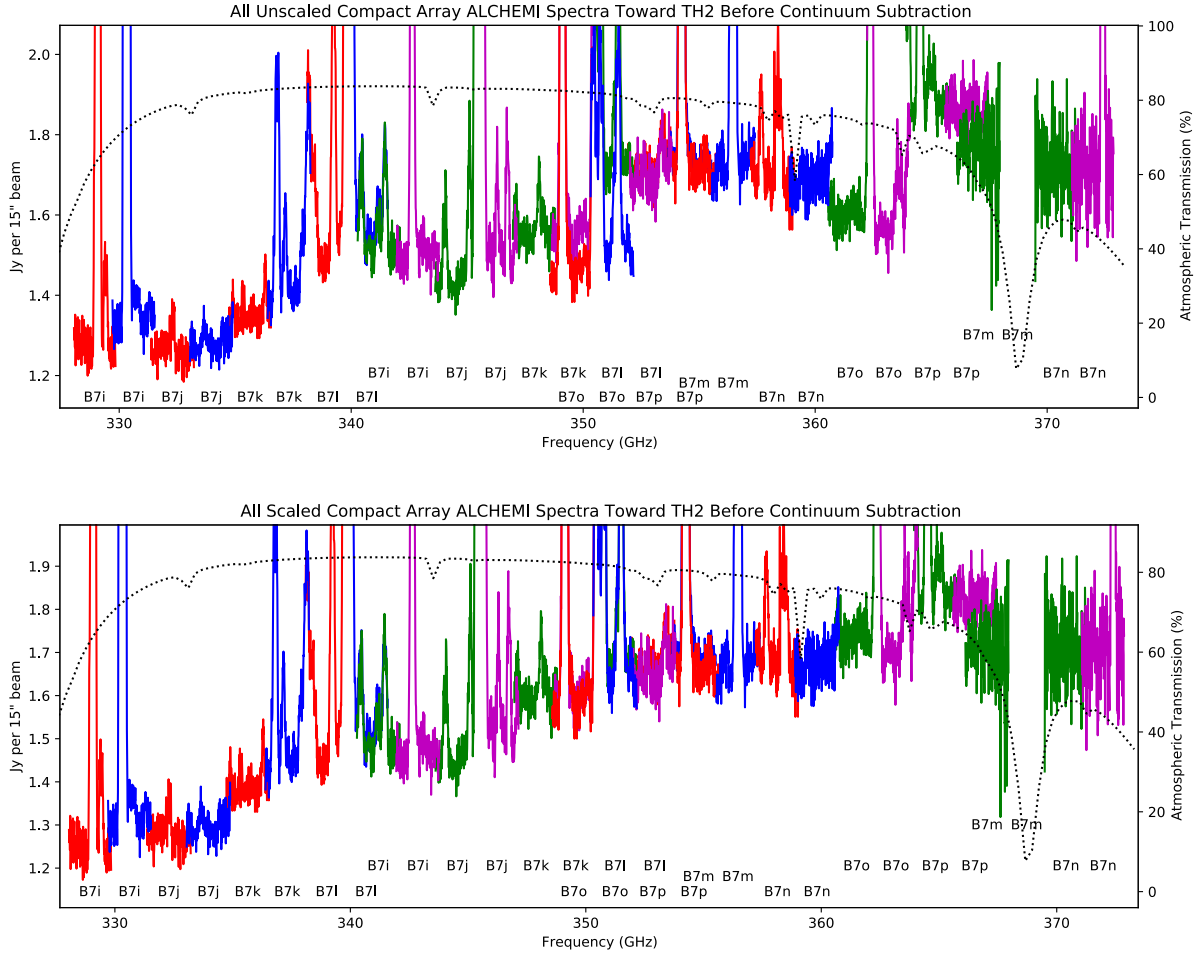

Fig. B.7. Same as Fig. B.2 but for the second half of Band 7 unscaled (top) and scaled (bottom).

Appendix C: ALCHEMI Flux Calibration

The ALMA flux calibration process includes a number of contributions to its uncertainty, including systematic errors within a given measurement calibrated with a single primary flux reference such as that due to:

1. The primary flux calibrator model used to set the absolute flux calibration scale.
2. The primary flux calibrator measurement used to define the reference point for the secondary flux calibrator flux.

as well as random uncertainties due to:

1. The bootstrapping from the primary to the secondary flux calibrator.
2. The bootstrapping from the secondary flux calibrator to the target source.
3. The lack of a proper elevation-dependent opacity correction during any of the bootstrapping steps.

Furthermore, even though extra mitigation measures can be done during an observation to account for items 4 and 5 above, there is nothing that can allow one to attain an absolute flux calibration error that is better than the error associated with the primary flux calibrator measurement and model.

Early in the process of imaging the ALCHEMI measurements, amplitude offsets between overlapping receiver tunings were noted (see Sect. 3.1 and Appendix B). The analysis of these offsets has given ALCHEMI the ability to correct for "at least one component" of the flux calibration uncertainty. This flux calibration alignment, though, does not allow for the determination of the absolute flux calibration reference. At best we have corrected the flux scales within our individual scheduling blocks to a common value. The ALCHEMI image cubes have been corrected for these flux rescaling factors, which we believe has corrected for noise introduced as part of the flux calibration process after the primary flux calibrator measurement.

In the following we address two levels of flux calibration uncertainty in the ALCHEMI data: Relative flux calibration, which represents the flux calibration uncertainty to be used when comparing fluxes within the ALCHEMI image cubes for a given set of imaging inputs (i.e., array, spatial, and spectral resolution); Absolute flux calibration, which represents the flux calibration uncertainty to be used when comparing fluxes derived from the ALCHEMI image cubes for comparison with other (non-ALCHEMI) measurements.

C.1. Relative Flux Calibration Uncertainty

The spectral flux normalization that we have applied to all ALCHEMI measurement sets has effectively normalized all ALCHEMI data to a common flux calibration scale for each array configuration[5] measured in the ALCHEMI survey. This implies that we have normalized all ALCHEMI data measured with a given array configuration to the same relative flux calibration scale. This furthermore implies that comparison of spectral lines within the ALCHEMI survey can be compared using a relative flux calibration uncertainty.

The statistics of the amplitude scaling factors given in Table A.1 are provided in Table C.1. It is noteworthy that for our Band 3 measurements the 12mE configuration shows significant deviations from the average values of the scaling factors for that receiver band and configuration.

An estimate of the relative flux calibration uncertainty associated with a given receiver band and configuration can be derived from the scatter in the scaling factors (Table C.1) that we have applied to our measurement sets to normalize them to the same mean flux scale. The RMS values for the flux scale normalization factors for each Band and array configuration(s) (listed as Compact Array / Extended Array / Combined) are:

- Band 3: 2% / 12% / 12%
- Band 4: 1% / 2% / 2%
- Band 5: 2% / 2% / 2%
- Band 6: 5% / 1% / 5%
- Band 7: 8% / 3% / 9%

The relative flux calibration uncertainty for the ALCHEMI image cubes which are combinations of the Compact Array and Extended Array measurements will in reality be a complex combination of the relative flux calibration uncertainties, which itself depends upon the contribution of each array measurement to a given flux in the ALCHEMI survey. The contribution of each array to the combined measurement is dependent upon numerous factors such as relative visibility contributions and time-dependent variations between the individual array measurements. In the above, we conservatively estimate the relative flux calibration uncertainty for the combined values as the root-sum-square of the Compact Array and Extended Array scaling factor RMS values.

Be aware that the actual "flux uncertainty" to be used in a line-ratio analysis, for example, is not determined solely by the "flux calibration uncertainty" in complex sources such as NGC 253. The line flux one measures depends on how the imaging process (robust parameter, clean mask, clean depth, selfcal, *etc.*) has been performed and on the properties of the spectral line itself. The same imaging parameters can have different effects on different spectral lines. For example, when different spectral lines have distinct spatial extents or when one spectral line is bright and the other is faint because the brighter spectral line has a larger fraction of its flux cleaned. For these reasons, the real flux calibration uncertainty is likely to be larger than that assumed from an assessment of the quality of the flux calibration process alone.

C.2. Absolute Flux Calibration Uncertainty

The absolute flux calibration uncertainty starts with the relative flux calibration uncertainty and includes contributions due to the measurement, model, and application of the primary flux calibration source (see above). To estimate this additional contribution, we assume that the measurement of the relatively bright sources used as primary flux calibrators provide a negligible contribution to the primary flux calibration uncertainty. This uncertainty is then dominated by that associated with the primary flux calibrator model. Models used by ALMA within CASA are unlikely to be accurate to <5% (Butler 2012, priv. comm.). We use then the following recommendations for flux calibration accuracy, from the ALMA Proposer's Guide for Cycle 5[2] (Section A.9.2 on "Flux Accuracy"), as an estimate of the primary flux calibrator model uncertainty:

- Bands 3, 4, 5: < 5%
- Bands 6, 7, 8: < 10%
- Bands 9 and 10: < 20%

The absolute flux calibration uncertainty, including the relative flux calibration uncertainty derived for the ALCHEMI image cubes, is given by the root-sum-squared of the relative

[5] By array configuration we mean to differentiate among the Compact Array, either ACA (7m) or 12m Compact (12mC), the Extended Array (12m/12mE) and Combined (12m7m/12mE12mC) that were used for each spectral setup. Each of these observations consisted of a number of individual observations with slightly varying array configurations depending on the antenna availability at the time of the observation.

Table C.1. Statistics by bands and arrays of the relative flux scaling factors (a_i)

Band	Array	N_{obs}[a]	Average $\overline{a_i}$	RMS σ_{a_i} (%)	min(a_i) / max(a_i)	max(a_i)-min(a_i) (%)
B3	12mC	6	0.989	2.4	0.937 / 1.009	7
B3	12mE	6	1.000	12.4	0.789 / 1.123	34
B4	7m	7	1.000	1.3	0.980 / 1.021	4
B4	12m	7	1.000	1.7	0.968 / 1.026	6
B5	7m	8	1.000	2.3	0.955 / 1.033	8
B5[b]	12m	8	0.911	2.3	0.856 / 1.147	29
B6	7m	10	0.974	4.7	0.867 / 1.027	16
B6	12m	10	1.003	1.2	0.990 / 1.034	4
B7	7m	16	1.006	8.1	0.833 / 1.257	42
B7	12m	16	1.001	2.5	0.956 / 1.044	9

Notes. [(a)]Total number of scheduling block measurements included in the subsequent statistics shown. [(b)]Excludes 12m Array SB B5f as the scaling factor for this SB appears to include amplitude calibration errors inherent in the delivered calibrated data products.

and primary flux standard model calibration uncertainties (listed as in Sect. C.1):

- Band 3: 5% / 13% / 13%
- Band 4: 5% / 5% / 5%
- Band 5: 5% / 5% / 5%
- Band 6: 11% / 10% / 11%
- Band 7: 13% / 10% / 13%

Therefore, for the sake of simplicity, we recommend the usage of a conservative 15% uncertainty for the absolute flux calibration within the ALCHEMI image cubes, at any frequency and configuration.

C.3. A Search for the ALCHEMI Flux Normalization Anomalies

We find that 11 of the 47 tunings (~23%) which comprise the ALCHEMI data set have amplitude scale factors which are larger than the ALMA amplitude calibration specification of 5%, with the two most discrepant tunings being 26% (Band 7) and 21% (Band 3). Table C.2 lists the measurement information for the 11 discrepant tunings.

In an attempt to determine the source(s) of the thirteen science goals with poor amplitude calibration, we have investigated how ALMA calibrates amplitude within the limits of the information provided to investigators. ALMA flux calibration is made within a given observation (or "execution block") by measurement of a standard quasar selected from a list of monitored quasars, referred to as the "grid sources". ALMA strives to measure these standard quasars at least once every 14 days at bands 3 and 7, and calibrates their fluxes to an absolute scale through reference measurements of primary flux calibrators (i.e., Uranus). The measured absolute fluxes for the grid source calibrators are available from the ALMA calibrator archive. We have extracted the flux scaling information from the calibration pipeline weblog file "flux.csv" associated with each observing execution block (EB). This flux scaling information includes the "spectral index age" and time since the standardized flux for each calibrator was derived.

C.3.1. Possible Source of Error: Large Spectral Index Age (spixAge)

As the spectral index age (spixAge) is one of the factors used by getALMAFlux to extrapolate measured flux calibrator fluxes to target frequencies, there was a concern that perhaps large spixAge factors were causing the large flux calibration errors. Using the spectral index age information extracted from the pipeline calibration process we show the correlation between spectral index age and amplitude scale factor in Figure C.1. There is no correlation between spixAge and the amount of the flux calibration error.

C.3.2. Possible Source of Error: Calibrator Catalog Band 3 Age

By inspecting the age of the absolutely calibrated Band 3 flux used by getALMAFlux (extracted from the flux.csv files associated with the pipeline calibration process), we find that there is no apparent correlation between the "Age"/"Band3Age" and large amplitude scaling factors. The "Age" or "Band3Age" is in almost all cases between 0 and 3 days for our most discrepant scale factor EBs. In one case it was 6 days, and another was 5 days, but neither of these were from our "worst cases". Band 3 age does not appear to be a likely source for the discrepant amplitude scale factors.

C.3.3. Possible Source of Error: Flux Monitoring Time Gaps

Many, though not all, of the science goals (SGs) with discrepant amplitude scale factors occur just after a gap in the respective flux calibrator measurements. Specifically, for 8 of the 13 discrepant Band 3 SGs, there was a significant flux calibrator measurement time gap just before these SGs were observed, and this correlation between flux calibrator measurement time gap and discrepant scale factor does not exist for Band 6 (green) or Band 7 (black) SGs with discrepant amplitude scale factors. Although this may be an explanation for the excessive Band 3 flux calibration uncertainties, a time gap in the flux monitoring for our flux calibrators does not appear to be consistent for all SGs with discrepant flux calibration.

C.3.4. Possible Source of Error: Large Time Span Between System Temperature Measurements

By perusing the weblogs associated with the ALCHEMI measurements we know that the scaling from raw amplitude to a temperature scale (otherwise known as the "system temperature" measurement), was routinely made only every ~11 minutes

Table C.2. ALCHEMI tunings with discrepant amplitude calibration

SG[a]	Array	Flux Calibrators	SpixAge[b]	$100 \times \left\lvert \frac{\sigma_{gain}}{S_{gain}} \right\rvert^{c}$	$a_i{}^{d}$
B7d	7m	J2258−2758,J0006−0623,J0522−3627	(3,-4,20),(-4,20),20	9.98	1.257
B3b	12mE	J2258−2758	142,144	0.86	0.789
B7h	7m	J2258−2758,J2253+1608,J0522−3627	(3,4),25,4	9.87	0.833
B6f	7m	J2253+1608	-1,0,6	1.98	0.867
B3d	12mE	J0006−0623	7	1.57	1.128
B3a	12mE	J0006−0623	-5,4	0.05,0.68	1.108
B3c	12mE	J0006−0623	-3,-6,0,1	0.48	1.107
B7o	7m	J2253+1608,J0522−3627	(7,0,2,3),2	2.06	0.922
B3f	12mE	J2258−2758,J2357−5311,J0006−0623	-27,-22,4	1.84	0.922
B6h	7m	J2258−2758	5,-3,0,-2	3.71,1.03,1.20,4.30	0.924
B3a	12mC	J0006−0623	23,27	0.24	0.937

Notes. [a]Refers to Science Goals within ALMA project nomenclature. [b]Number of days since the most recent ALMA-derived spectral index for a given calibrator. Multiple executions which used a given calibrator are grouped within parentheses. Negative values indicate spectral indices derived before a given calibrator measurement. Calibrator spectral indices are derived using measured Band 3 and Band 6 or Band 7 fluxes. [c]Normalized gain calibrator flux uncertainty averaged over all gain calibrator measurements for observation dates within five days. Multiple entries indicate multiple observation time ranges. Target for all gain calibration measurements was J0038−2459. [d]Amplitude scale factors are applied to the data as indicated by Equation 3.

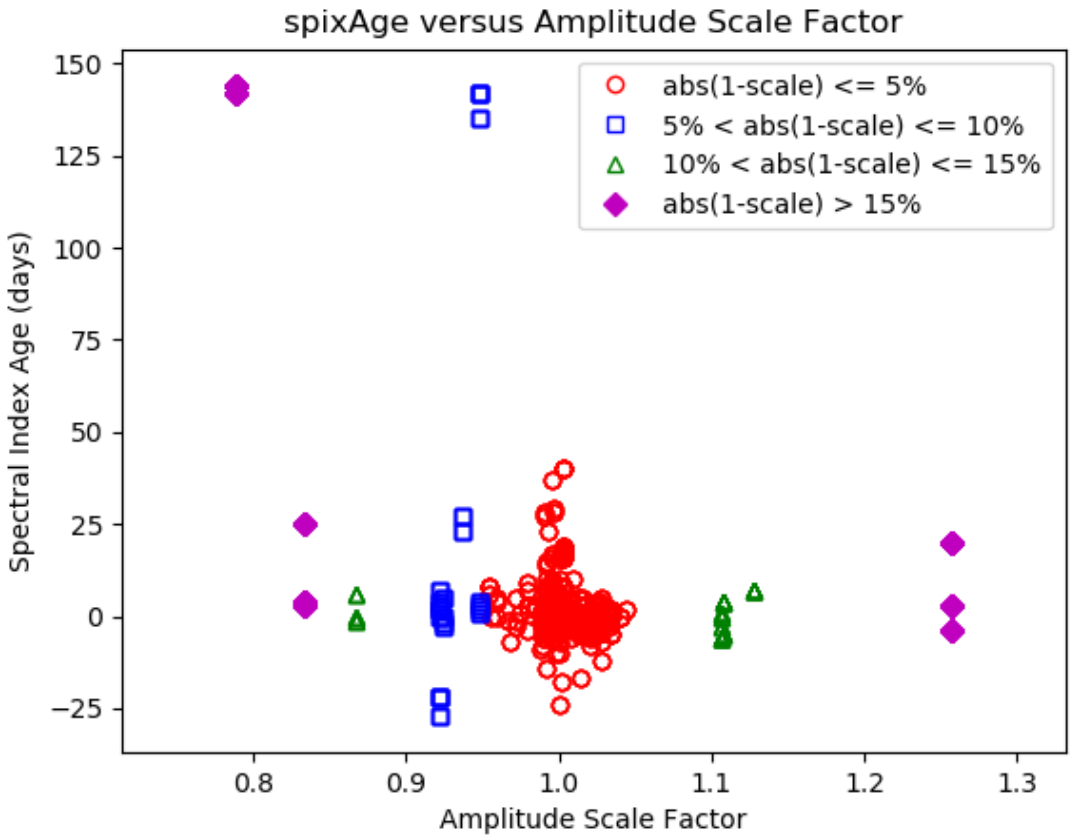

Fig. C.1. Correlation between spectral index age and amplitude scale factor for all ALCHEMI measurements. Coloring is used to designate ranges of amplitude scaling.

at Band 3 and every ∼8 minutes at Band 7. As these system temperature measurements are required to track the changes in sky emission as a function of time, it could be that these basic amplitude scaling factors have not been sampled well enough in time, especially at the higher frequency bands. However this is an observatory trade-off between enhanced calibration accuracy and observing efficiency.

C.3.5. Possible Source of Error: Noisy Gain Calibrator Measurement

For the SG with the most discrepant flux calibration, B7d 7m (ngc253_d_07_7M) there may be an issue with gain calibrator phase stability. Three out of five execution blocks (EBs) for the scheduling block (SB) were taken on the same day

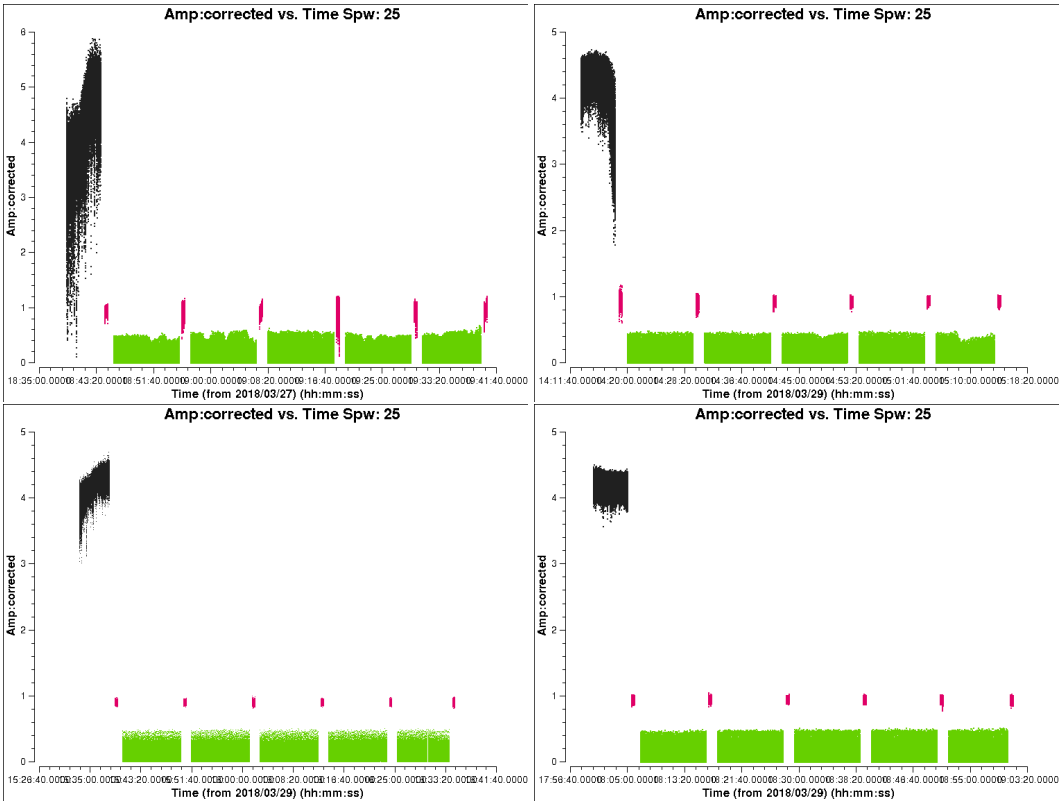

Fig. C.2. B3b 7m amplitude/bandpass calibrator flux versus time weblog plots for the four EBs in this SB.

(2018-01-21). J0038−2459 was observed as the gain calibrator for all the three EBs. Although the gain calibrator flux is expected to be stable over the three EBs, because the flux is very likely to be stable over the short time scale between these three EBs (about six hours), the derived flux densities in the pipeline calibration changed about 28% (peak-to-peak). The following is a summary of the pipeline-derived flux densities of the phase calibrator (reference: the weblog, stage 15).

```
# EB                        start date/time (UT)
 flux density (spw 16)
uid___A002_Xc96f17_X8658   2018-01-21 19:06:14
 1024.0+-9.979 mJy
uid___A002_Xc96f17_X8ec1   2018-01-21 22:17:40
 855.121+-12.804 mJy
uid___A002_Xc96f17_X92b9   2018-01-21 23:53:08
 797.500+-5.496 mJy
```

It is possible that poor atmospheric phase stability is the cause of the large flux calibration uncertainty, as all the EBs were taken in the late afternoon to early evening, which is the part of the day when the atmospheric phase stability tends to be very the poorest. In fact, in the calibrated visibility amplitude vs time plot of the EB (weblog stage 17) one can see frequent amplitude drops in the Bandpass/Flux calibrator scan.

Another example of a correlation between poor phase stability and poor flux calibration is B3b 12mE (ngc253_b_03_TM1). As was the case for B7d 7m, the EBs for this SB were also affected by large phase fluctuations, and that they were also executed in daytime (late afternoon). Figure C.2 shows the pipeline plots of amplitude vs time for all the EBs for B3b 7m. Significant amplitude drops in the bandpass/amplitude calibrator (J2258−2758) can be seen especially in EB uid___A002_Xcb1740_X94c9, and they could affect the flux scaling of the gain calibrator.

The following is a summary of the pipeline-derived flux density of gain calibrator J0038−2459 (reference: the weblog, stage 15).

```
spw=25
uid___A002_Xcb1740_X94c9   2018-03-27 18:36:03
 955.851+-14.748 mJy
uid___A002_Xcb339b_X600b   2018-03-29 14:10:14
 938.721+-7.809 mJy
uid___A002_Xcb339b_X633f   2018-03-29 15:30:21
 903.452+-9.069 mJy
uid___A002_Xcb339b_X68ab   2018-03-29 17:57:08
 941.212+-1.904 mJy
```

The change of delivered flux density looks relatively large (5.8% in peak-to-peak) even though the EBs were taken within three days. This could be an explanation for the discrepant flux calibration (second worst of all SGs) for this SG.

In order to assess the effect of a large gain calibrator flux uncertainties on the derivation of our flux calibration uncertainty for all of the ALCHEMI SGs, we have extracted all derived gain calibrator fluxes and uncertainties from the ALCHEMI weblogs. We have derived a normalized gain calibration error for each SG by doing the following: Firstly, we calculate the weighted uncertainty (σ_{gain}) for all gain calibrator measurements; Secondly, we average normalized gain calibrator uncertainties ($\frac{\sigma_{gain}}{S_{gain}}$) over all spectral windows and measurements taken within 5 days of each other. This time window is expected to be shorter than any changes in the absolute flux of the gain calibrator; Finally, by using a normalized gain calibrator uncertainty, we are attempting to smooth-out any changes in gain calibrator flux measurement uncertainty due to differences in gain calibrator integration time.

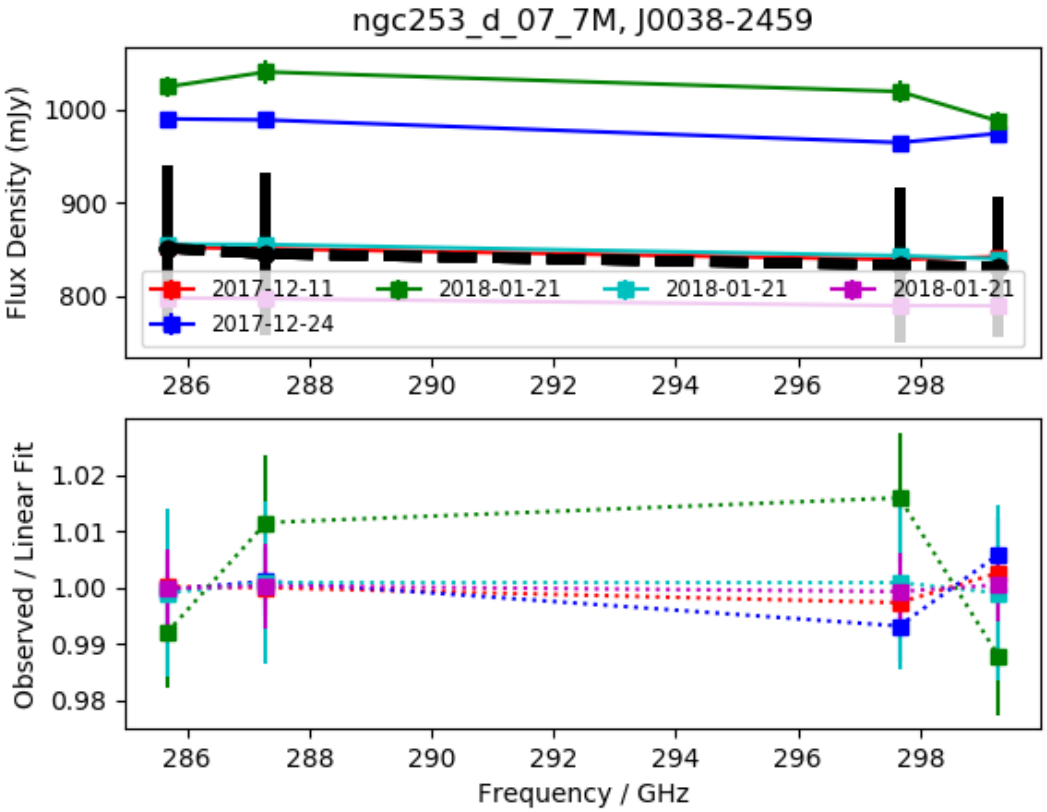

Fig. C.3. Sample gain calibration results for all EBs associated with B7d 7m. The bottom panel shows the residual from a linear fit for each measurement date to the measured flux densities displayed in the top panel.

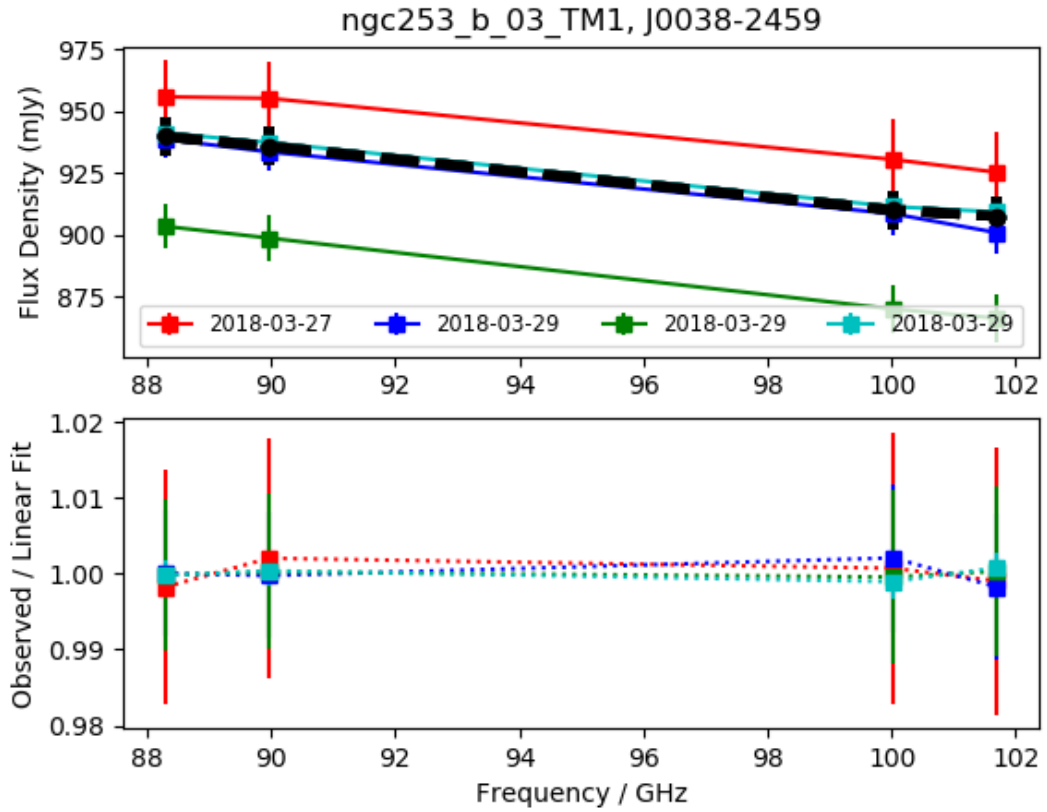

Fig. C.4. Sample gain calibration results for all EBs associated with B3b TM1. Same diagram style as used in Figure C.3.

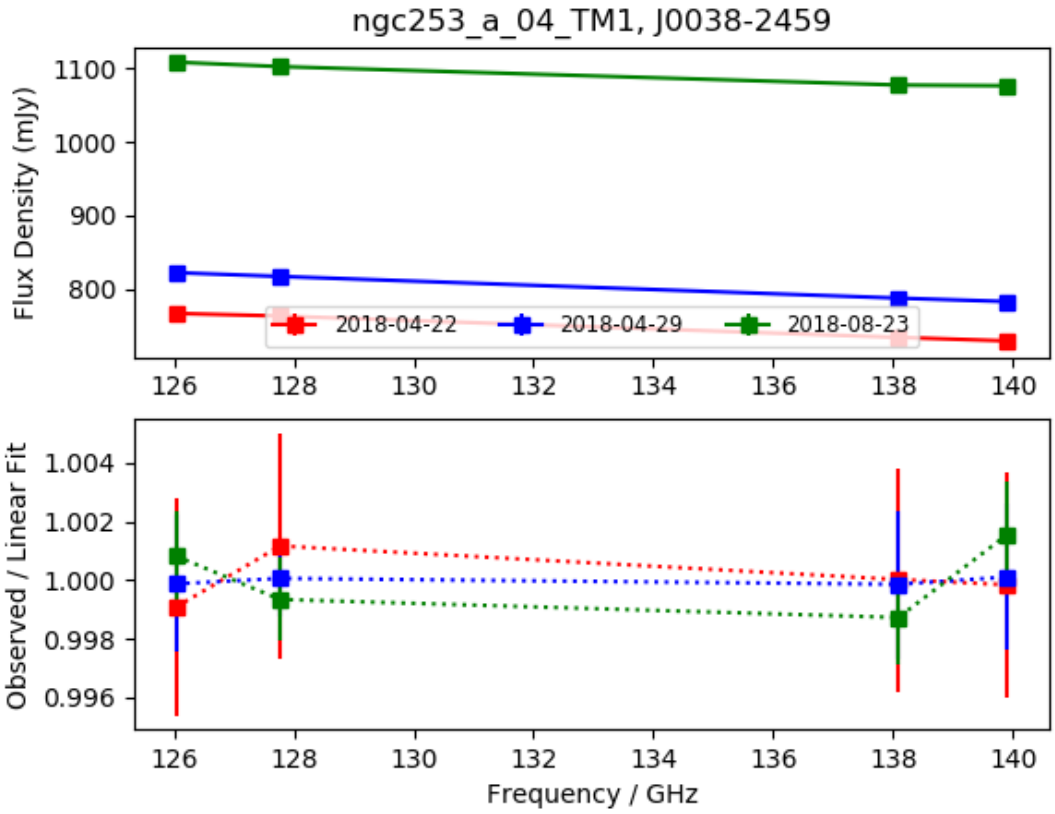

Fig. C.5. Sample gain calibration results for all EBs associated with B4a TM1. Same diagram style as used in Figure C.3.

Figures C.3, C.4, and C.5 show examples of gain calibrator measurements, with weighted uncertainties, and their associated weighted average as a function of frequency. Figure C.6 shows the correlation between normalized gain calibrator standard deviation (as a percentage) versus the associated amplitude calibration scale factor (calculated as a difference from a perfect amplitude scale factor of 1.0). Even though in a few cases large normalized gain calibration errors are associated with large amplitude scale factors, there is no systematic correlation between these measures.

C.4. Conclusion to Search for ALCHEMI Flux Normalization Anomalies

In Sections C.3.1 through C.3.5 we have investigated the possible sources of the discrepant flux calibration uncertainties derived for 13 of the ALCHEMI SBs. We find that with the exception of possible errors in T_{sys} measurement, which we are unable to properly analyze, none of the above potential sources of error appear to explain all of our discrepant amplitude calibration.

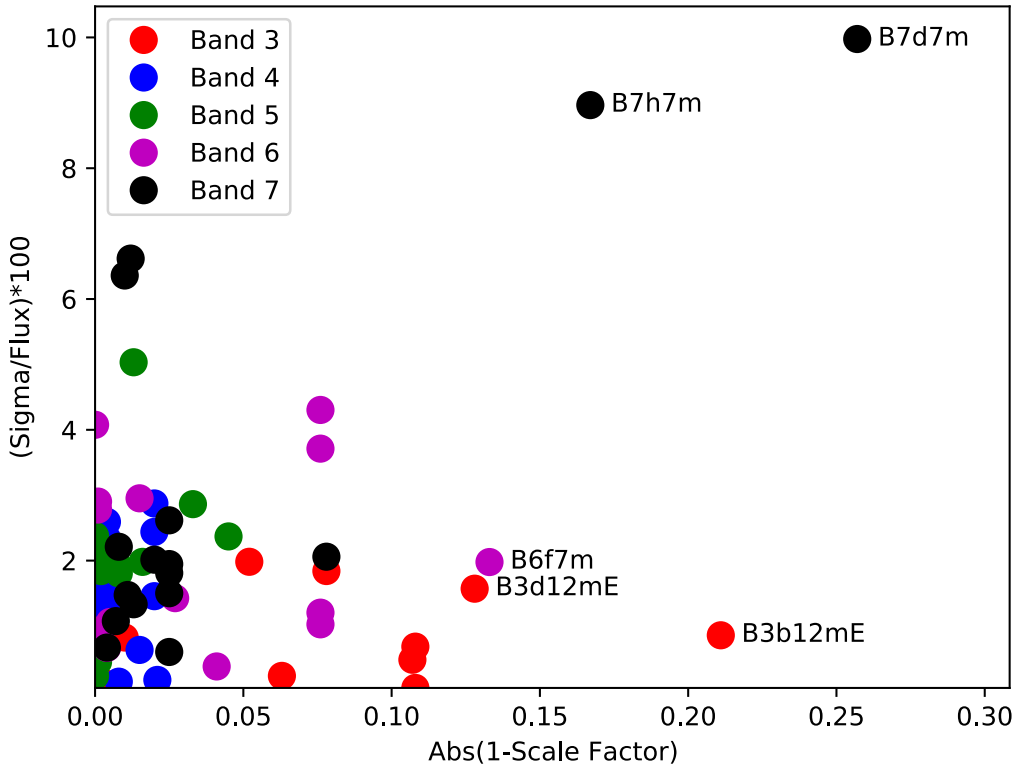

Fig. C.6. Correlation between normalized gain calibrator standard deviation (as a percentage) versus the associated amplitude calibration scale factor (calculated as a difference from a perfect amplitude scale factor of 1.0). Tunings with larger than 12% scale factors are annotated. See above description for calculation details.

Appendix D: Fitting details of individual species

Sect. 4.3.2 provided details on the procedure used to fit the modeled synthetic spectra to the low resolution ACA observations. In summary, the procedure consists on a human-supervised automatic fit, where the only intervention aims at ensuring convergence of the fit. Additional criteria used for the newly detected species (Sect. 4.4) are provided below in Sect. D.1. Thus, parameters were fixed or transitions were masked in the fit when convergence could not be achieved. The results are reported in Table. A.3. Here we note that in some cases, the large uncertainty in the fit to the temperature resulted in column density errors of the same order as the value fitted. Such is the case of $H^{13}CN$, despite being a clear detection with bright features, extra masking and fixing of the temperature was required to provide a reasonably narrow error on the column density (with only marginal change in the fitted column density value). However in most cases we decided to maintain such fits for the sake of consistency with the procedure applied to all species.

Although we know from previous studies that there is evidence for the presence of multiple components with different excitation temperatures (Aladro et al. 2011b), there are no really obvious deviations from the LTE fit. As an example the higher energy transitions of HC_3N appear to be underestimated, which could support the presence of a higher temperature component. Similarly H_2CO is not that well fitted under LTE, showing flat topped spectral features. For the sake of simplicity in the presentation of these data, we assumed a single LTE component for all species. A detailed analysis of the excitation of some of these species will be presented in future publications which will make use of the higher resolution ALCHEMI 12m Array data.

For the sake of completeness, a list of all transitions above a peak flux density of 15 mJy are presented in Table D.1. We note that these intensities correspond to those of the model fit to the observed spectra, and therefore parameters of velocity and width are those corresponding to the species as presented in Table A.3. As indicated in Sect. 4.3.2, no measurement or analysis of individual spectral features has been performed. For the reasons presented there, analysis has been performed per molecular species.

Below we provide some cases of transitions significantly deviating from LTE together with other special details on the fitting of individual species.

H_3O^+ : The fit to H_3O^+ emission has been performed only on the 307.2 GHz transition, which is one of the two transitions covered by our survey. Although the 307.2 GHz is blended with CH_3OH, this contribution is accounted for based on the CH_3OH fit to the whole survey. The 364.8 GHz transition, on the other hand, is the most obvious case of non-LTE emission, and is observed to be more than an order of magnitude brighter than predicted by LTE (Fig. F.11) The line ratio between these two transitions has been calculated based on the individual integrated intensity fit to each transition and not on the LTE intensities in Table. D.1. To explain the relatively large observed flux density ratio of $S_{364.8}/S_{307.2} = 6.8 \pm 1.0$ between the two transitions, non-LTE models from Phillips et al. (1992) suggest volume densities $< 10^7 cm^{-3}$ and effective excitation by dust emission. Together with the vibrational emission reported in Sect. 5.2, H_3O^+ is also probing the importance of infrared pumping in NGC 253 GMCs. However, the 396 GHz transition of H_3O^+, not covered in our survey, is key to constrain the non-LTE physical conditions of the emitting gas. All other species below that show transitions not well fitted by the LTE approximations, are not as extreme as the case of H_3O^+ where, as mentioned

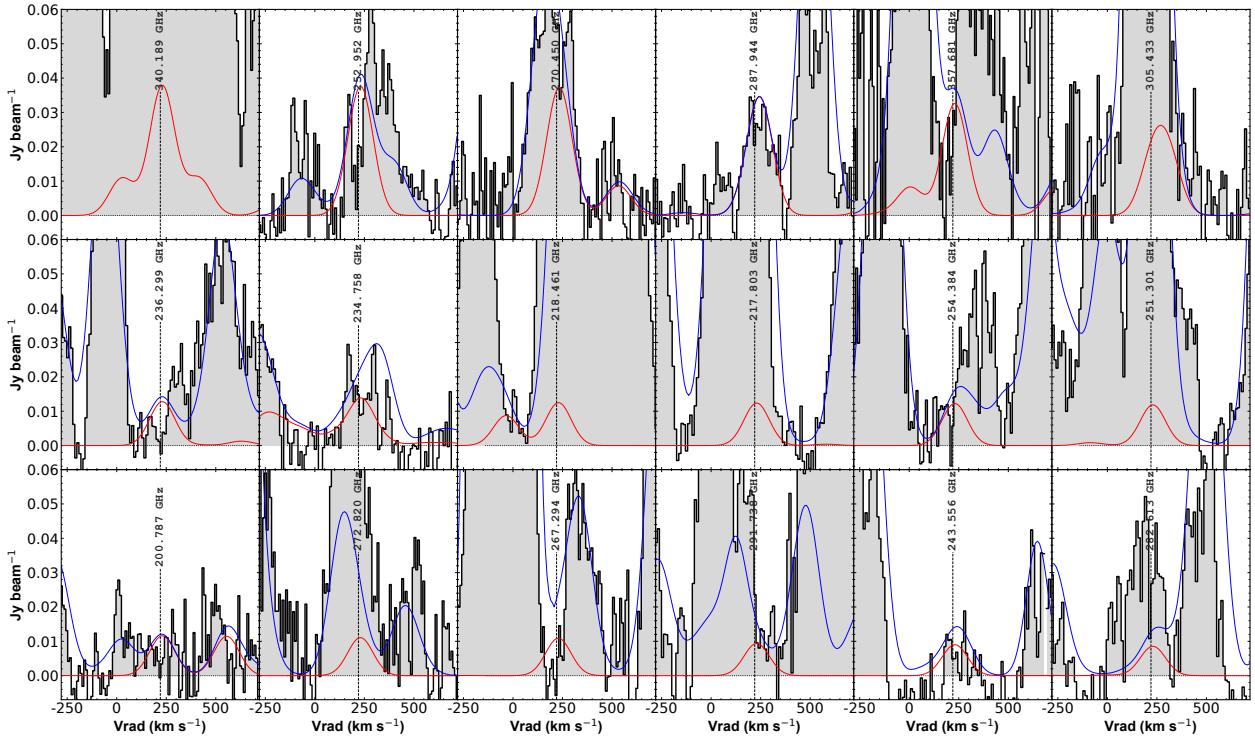

Fig. D.1. Modeled emission of C_2H_5OH in red, overlaid over the observed spectrum (filled black histogram) and the global model including all molecular transitions in this study. Only the 18 brightest transitions or group of transitions according to the LTE model of C_2H_5OH are displayed, ordered in descending order of brightness from left to right and top to bottom. The model generated with MADCUBA makes use of the spectroscopic parameters in JPL catalog entry 46004. The frequency of the brightest transition in each panel are displayed for reference.

above, the LTE approximation is underestimating the 364.8 GHz by more than an order of magnitude.

H_2S : The transition of H_2S at 216.71 GHz is approximately two times brighter than predicted by the LTE fit.

H_2CO : The transitions at 140.83 and 150.48 GHz are twice as bright as predicted by the LTE fit. A number of other transitions also deviate from the fit, but to a lesser extent. We note that we did not fit the ortho- and para-H_2CO separately, but we assumed the ortho-to-para ratio of 3.

HC_3N : All transitions above 270 GHz are brighter than the LTE fit estimate. This could be the signature of a warmer component and partially to the effect of varying opacity across the transitions.

$HNCO$: The brighter transitions of HNCO show an obvious double peak profile which is likely due to the distribution of this species at high resolution (Meier et al. 2015). This double peak profile, similarly observed in CH_3OH, is more apparent than in other species where the velocity components are more blended and the profile is a single peak. On the other hand, many of the fainter transitions of HNCO are overestimated by the LTE fit.

$CH_3^{13}CCH$: Despite being almost uniformly blended with other species, the fit of $CH_3^{13}CCH$ is consistent within the errors to that of the other two isotopologues, being ∼0.1 dex above $CH_3C^{13}CH$ and ∼0.4 dex above $^{13}CH_3CCH$. Although the uncertainties in the column density determination of the latter two isotopologues are of the same order as the value fitted, an independent fit to the three isotopologues are in good agreement, which supports the detection and fit to those species. Moreover, the ratio to the main isotopologue (Table 4) is consistent with what is observed with other species as discussed in Sect. 5.4.1).

CH_3OH : Two of the transitions of methanol, the $1_{1,0}-2_{0,2}$ at 205.79 GHz and $7_{1,7}-6_{1,6}$ at 335.58 GHz, show observed fluxes which are less than half of the LTE fit flux, while the $6_{1,5}-5_{1,4}$ at 292.7 GHz transition is about half of the LTE fit flux. Similar to what is observed in HNCO, the brighter transitions show a very clear double peak profile.

$^{13}CH_3OH$: There is only one transition of $^{13}CH_3OH$ which is bright enough and is not blended with other species. Therefore this is the only species in which the fit value should be considered with caution and probably an upper limit. This LTE fit has been discussed in Sect. 5.4.1.

CH_3CN : The $J = 7-6$ and $8-7$ groups of transitions at 128.7 and 147.1 GHz, respectively, show significantly brighter emission than that from the LTE fit, being up to a factor of two brighter on the former.

CH_2NH : While the $3_{1,1}-1_{0,1}$ transition at 166.85 GHz is not detected, though predicted by the LTE fit, the $2_{0,2}-1_{0,1}$ transition at 127.85 GHz is brighter than predicted.

D.1. Fitting details of newly detected species

On top of the fit criteria explained in Sect. 4.3.2 on detection of the brightest spectral features and requiring convergence of the fit, we enforced extra criteria to claim newly detected species. This is, at least one of the brightest (according to the LTE prediction) spectral features needs to be un-blended or marginally contaminated by emission from other species based on the LTE modeling to other transitions from the contaminant species. More importantly, all other blended transitions should be consistent with the residual spectra after subtraction of all other modeled species. In other words, any bright emission line predicted

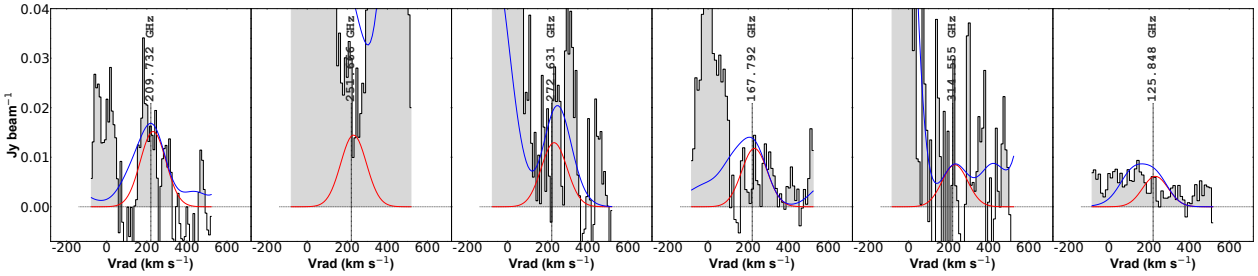

Fig. D.2. Same as Fig. D.1 showing the model of HOCN, using the spectroscopic parameters in CDMS catalog entry 43510.

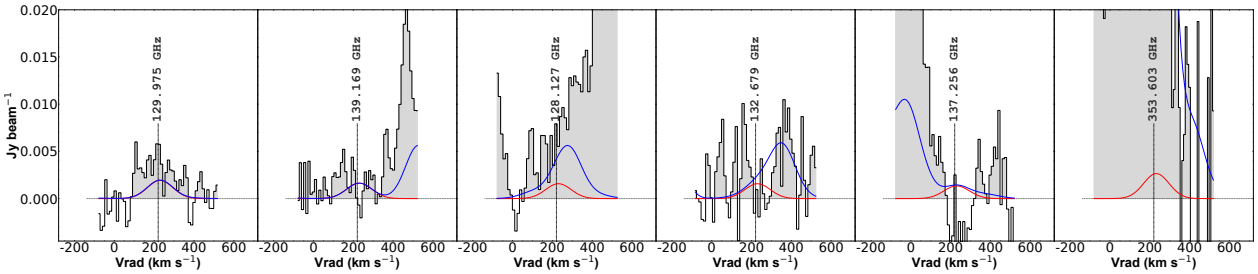

Fig. D.3. Same as Fig. D.1 showing the model of HC_3HO, using the spectroscopic parameters in JPL catalog entry 54007.

Table D.1. Intensities from the 744 transitions with > 15 mJy from the LTE model fit to the data

Formula	ν (GHz)	S (mJy)	Formula	ν (GHz)	S (mJy)	Formula	ν (GHz)	S (mJy)	Formula	ν (GHz)	S (mJy)
Hβ	126.794	24	HNCO	198.529	22	Hα	256.302	86	Heα	316.544	32
HC_3N	127.368	213	HNCO	198.529	25	CH_3C_2H	256.317	71	CH_2NH	317.405	64
CH_3CN	128.779	29	HNCO	198.529	28	CH_3C_2H	256.332	120	CH_2NH	317.405	78
SO	129.139	27	CH_2NH	199.823	34	CH_3C_2H	256.337	142	c-C_3H_2	318.294	34
SiO	130.269	71	HC_3N	200.135	189	Heα	256.406	27	CH_3OH	318.319	74
HNCO	131.886	59	H_2C_2N	201.144	31	^{29}SiO	257.255	20	c-C_3H_2	318.482	93
HNCO	131.886	49	CH_3CN	202.34	35	CH_3CN	257.508	39	c-C_3H_2	318.79	30
HNCO	131.886	41	CH_3CN	202.356	77	CH_3CN	257.527	83	HC_3N,v7=1	319.576	36
CH_3OH	132.891	15	H_2CS	202.924	39	$HC^{15}N$	258.157	63	NH_2CN	321.93	19
C_3H^+	134.933	22	c-C_3H_2	204.789	19	SO	258.256	150	CH_3OH	322.239	35
Hβ	135.249	26	CH_3C_2H	205.045	53	$H^{13}CN$	259.012	105	C_2H_5OH	322.691	21
Hα	135.286	50	CH_3C_2H	205.065	64	$H^{13}CN$	259.012	152	C_2H_5OH	322.691	21
Heα	135.341	15	CH_3C_2H	205.077	108	$H^{13}CN$	259.012	71	CH_3NH_2	323.462	16
HC_3N	136.464	231	CH_3C_2H	205.081	129	Hβ	260.033	46	^{13}CS	323.685	19
CH_3C_2H	136.705	21	Hβ	205.76	38	$H^{13}CO^+$	260.255	339	CH_3C_2H	324.607	42
CH_3C_2H	136.718	27	CH_3OH	205.791	272	SiO	260.518	193	CH_3C_2H	324.638	49
CH_3C_2H	136.725	47	H_2CS	205.987	21	CH_3NH_2	261.219	34	CH_3C_2H	324.657	81
CH_3C_2H	136.728	56	SO	206.176	98	$HN^{13}C$	261.263	173	CH_3C_2H	324.663	97
SO	138.179	73	OCS	206.745	35	NH_2CN	261.594	20	CH_3NH_2	325.531	50
^{13}CS	138.739	34	CH_2NH	207.38	15	CH_3OH	261.806	128	^{13}CN	325.943	30
H_2CO	140.84	135	NS	207.436	30	SO	261.844	264	^{13}CN	325.956	21
H_2C_2N	140.84	36	NS	207.835	39	C_2H	262.004	1153	^{13}CN	325.958	31
CH_3OH	143.866	33	NS	207.838	24	C_2H	262.006	876	^{13}CN	326.119	42
Hβ	144.474	28	C_2S	208.216	15	C_2H	262.065	837	^{13}CN	326.125	19
$C^{34}S$	144.617	92	H_2CS	209.2	41	C_2H	262.067	555	^{13}CN	326.142	57
c-C_3H_2	145.09	48	HC_3N	209.23	167	C_2H	262.079	76	^{13}CN	326.143	33
CH_3OH	145.094	40	HOCN	209.732	15	C_2H	262.208	70	CH_3OH	326.631	15
CH_3OH	145.097	49	Hα	210.502	74	HNCO	262.77	26	CH_3OH	326.961	15
CH_3OH	145.103	69	Heα	210.588	23	HNCO	262.77	24	OCS	328.298	25
CH_3OH	145.126	15	H_2CO	211.211	410	HNCO	262.77	22	HC_3N,v7=1	328.701	38
CH_3OH	145.132	26	CH_3OH	213.427	56	HNCO	263.749	117	CH_3NH_2	329.199	51
HC_3N	145.561	243	$HOCO^+$	213.813	18	HNCO	263.749	108	$C^{18}O$	329.331	4461
H_2CO	145.603	147	CH_3NH_2	215.108	26	HNCO	263.749	99	HNCO	329.665	63
$C^{33}S$	145.756	19	SO	215.221	115	HC_3N	263.792	52	HNCO	329.665	58
OCS	145.947	17	c-C_3H_2	216.279	155	CH_3NH_2	264.172	32	HNCO	329.665	55
CH_3OH	146.368	34	H_2S	216.71	98	HNCO	264.694	26	^{13}CO	330.588	13300
CS	146.969	880	CH_3OH	216.946	19	HNCO	264.694	22	CH_3CN	331.046	23
Hα	147.047	54	SiO	217.105	191	HNCO	264.694	24	CH_3CN	331.072	50
Heα	147.107	17	^{13}CN	217.303	44	HC_3N,v7=1	264.817	22	SO_2	332.505	19

Table D.1. continued.

Formula	ν (GHz)	S (mJy)	Formula	ν (GHz)	S (mJy)	Formula	ν (GHz)	S (mJy)	Formula	ν (GHz)	S (mJy)
CH_3CN	147.163	19	^{13}CN	217.436	19	CH_3OH	265.29	27	CH_2NH	332.573	39
CH_3CN	147.175	42	^{13}CN	217.467	41	HCN,v2	265.853	47	CH_2NH	332.573	31
$HOCO^+$	149.676	27	c-C_3H_2	217.822	69	HCN	265.886	6477	CH_3NH_2	333.839	17
NO	150.176	23	c-C_3H_2	217.822	207	CH_2NH	266.27	39	CH_3NH_2	334.712	17
H_2CO	150.498	158	c-C_3H_2	217.94	157	CH_2NH	266.27	30	CH_3OH	335.134	31
NO	150.547	23	c-C_3H_2	218.16	52	$H^{15}NC$	266.588	16	Hβ	335.207	55
c-C_3H_2	150.852	126	H_2CO	218.222	369	CH_3OH	266.838	117	CH_3OH	335.582	136
HNCO	153.292	18	HC_3N	218.325	144	HCN,v2	267.199	48	$C^{17}O$	337.061	617
HNCO	153.292	16	CH_3NH_2	218.409	23	OCS	267.53	37	CH_3NH_2	337.119	18
CH_3C_2H	153.791	30	CH_3OH	218.44	93	HCO^+	267.558	7021	$C^{34}S$	337.397	175
CH_3C_2H	153.805	37	NH_2CN	218.462	16	HOC^+	268.451	240	HC_3N,v7=1	337.825	40
CH_3C_2H	153.814	63	OCS	218.903	37	C_2H_5OH	270.444	18	H_2CS	338.081	49
CH_3C_2H	153.817	76	HNCO	218.981	29	C_2H_5OH	270.451	18	CH_3OH	338.124	147
HNCO	153.865	62	HNCO	218.981	26	H_2CS	270.521	56	c-C_3H_2	338.204	100
HNCO	153.865	72	HNCO	218.981	24	HNC	271.981	3903	CH_3OH	338.345	197
HNCO	153.865	84	$C^{18}O$	219.56	2380	HC_3N	272.885	40	CH_3OH	338.409	254
HNCO	154.415	16	HNCO	219.798	130	CH_3C_2H	273.373	58	CH_3OH	338.513	49
HNCO	154.415	19	HNCO	219.798	106	CH_3C_2H	273.399	68	CH_3OH	338.541	26
Hβ	154.557	29	HNCO	219.798	117	CH_3C_2H	273.415	114	CH_3OH	338.543	26
HC_3N	154.657	249	SO	219.949	217	CH_3C_2H	273.42	136	CH_3OH	338.56	15
c-C_3H_2	155.518	26	^{13}CO	220.399	7383	HC_3N,v7=1	273.945	24	CH_3OH	338.583	28
CH_3OH	156.602	53	HNCO	220.585	29	H_2CS	274.521	29	CH_3OH	338.615	106
CH_3OH	156.829	15	HNCO	220.585	24	$H_2{}^{13}CO$	274.762	35	CH_3OH	338.64	49
CH_3OH	157.049	28	HNCO	220.585	26	CH_3CN	275.894	36	CH_3OH	338.722	92
CH_3OH	157.179	44	CH_3CN	220.73	38	CH_3CN	275.916	78	CH_3OH	338.723	80
CH_3OH	157.246	60	CH_3CN	220.747	83	^{13}CS	277.455	37	SO	339.341	18
CH_3OH	157.271	50	H_2C_2N	221.254	20	CH_3OH	278.305	22	CN	339.447	52
CH_3OH	157.272	70	NH_2CN	221.361	17	CH_3OH	278.342	31	CN	339.476	74
CH_3OH	157.276	68	Hβ	222.012	40	H_2CS	278.886	58	CN	339.517	117
OCS	158.107	21	CH_3C_2H	222.129	58	N_2H^+	279.512	1339	CH_3NH_2	339.724	56
SO	158.972	46	CH_3C_2H	222.15	69	OCS	279.685	36	^{34}SO	339.858	16
Hα	160.212	58	CH_3C_2H	222.163	117	H_2CO	281.527	544	CN	340.008	214
Heα	160.277	18	CH_3C_2H	222.167	139	NH_2CN	281.708	20	CN	340.02	214
H_2C_2N	160.949	38	$C^{17}O$	224.714	323	HC_3N	281.977	30	CN	340.032	1639
NS	161.298	19	C_3H^+	224.868	15	Hβ	282.333	49	CN	340.035	651
NS	161.697	26	CH_2NH	225.554	51	c-C_3H_2	282.381	93	CN	340.035	1068
HC_3N	163.753	247	CH_2NH	225.556	17	HC_3N,v7=1	283.072	26	$C^{33}S$	340.053	33
CH_3OH	165.05	38	H_2CO	225.698	456	$H_2{}^{13}CO$	283.442	26	CH_3OH	340.141	32
CH_3OH	165.061	53	CN	226.287	57	Hα	284.251	94	C_2H_5OH	340.189	18
CH_3OH	165.099	55	CN	226.299	46	CH_2NH	284.253	27	C_2H_5OH	340.189	18
CH_3OH	165.19	48	CN	226.303	46	CH_2NH	284.254	152	CN	340.248	2129
CH_3OH	165.369	36	CN	226.315	110	CH_2NH	284.255	27	CN	340.248	1615
CH_3CN	165.556	25	CN	226.333	51	Heα	284.366	29	CN	340.249	1201
CH_3CN	165.569	55	CN	226.342	53	HNCO	284.662	23	CN	340.262	155
Hβ	165.601	31	CN	226.36	265	HNCO	284.662	21	CN	340.265	154
CH_3OH	165.679	23	CN	226.617	60	HNCO	284.662	19	CH_2NH	340.353	16
H_2S	168.763	265	CN	226.632	461	c-C_3H_2	284.805	50	CH_2NH	340.354	191
H_2CS	169.114	25	CN	226.66	1399	c-C_3H_2	284.998	132	CH_2NH	340.355	16
CH_3OH	170.061	57	CN	226.664	458	CH_3OH	285.111	32	CH_3NH_2	340.598	56
OCS	170.267	25	CN	226.679	565	HNCO	285.722	101	$HC^{18}O^+$	340.633	69
$HC^{18}O^+$	170.323	30	CN	226.874	1416	HNCO	285.722	93	SO	340.714	157
HCS^+	170.692	24	CN	226.875	2077	HNCO	285.722	86	CH_3OH	341.416	137
CH_3C_2H	170.876	39	CN	226.876	890	HNCO	286.747	23	CH_3C_2H	341.683	35
CH_3C_2H	170.893	47	CN	226.887	299	HNCO	286.747	19	CH_3C_2H	341.715	41
CH_3C_2H	170.902	80	CN	226.892	297	HNCO	286.747	21	CH_3C_2H	341.735	68
CH_3C_2H	170.906	96	HC_3N	227.419	122	CH_3OH	287.671	142	CH_3C_2H	341.741	81
$HOCO^+$	171.056	27	CH_3OH	229.759	25	C_2H_5OH	287.918	17	NH_2CN	342.038	17
$HC^{15}N$	172.108	32	CH_3OH	230.027	29	C_2H_5OH	287.945	17	CS	342.883	1138
SO	172.181	68	CO	230.538	56226	$C^{34}S$	289.209	228	H_2CS	342.944	26
$H^{13}CN$	172.677	15	OCS	231.061	38	CH_3OH	289.939	155	CH_3SH	343.048	15
$H^{13}CN$	172.677	20	^{13}CS	231.221	53	CH_3OH	290.07	207	$H_2{}^{13}CO$	343.326	32
$H^{13}CN$	172.678	46	Hα	231.901	80	CH_3OH	290.111	268	$HC^{15}N$	344.2	55
$H^{13}CN$	172.678	86	Heα	231.995	25	CH_3OH	290.185	50	SO	344.311	145
$H^{13}CN$	172.68	15	CH_3OH	234.683	19	CH_3OH	290.19	25	CH_3SH	345.021	15
HC_3N	172.849	239	CO^+	235.79	32	CH_3OH	290.191	25	$H^{13}CN$	345.34	298
HCO	173.377	19	CO^+	236.063	57	CH_3OH	290.21	15	CO	345.796	112202
$H^{13}CO^+$	173.507	194	HC_3N	236.513	102	CH_3OH	290.213	27	NS	345.823	20
SiO	173.688	141	H_2CS	236.727	50	CH_3OH	290.249	112	NS	345.824	15
$HN^{13}C$	174.179	98	HC_3N,v7=1	237.432	16	CH_3OH	290.264	50	NS	346.221	17
H_2CS	174.345	27	NH_2CN	238.316	18	CH_3OH	290.307	81	SO	346.528	236
C_2H	174.663	658	CH_3CN	239.12	39	CH_3OH	290.308	94	HC_3N,v7=1	346.949	42

Table D.1. continued.

Formula	ν (GHz)	S (mJy)	Formula	ν (GHz)	S (mJy)	Formula	ν (GHz)	S (mJy)	Formula	ν (GHz)	S (mJy)
C_2H	174.668	446	CH_3CN	239.138	85	CH_3C_2H	290.452	54	$H^{13}CO^+$	346.998	252
C_2H	174.722	382	CH_3C_2H	239.211	60	CH_3C_2H	290.48	63	SiO	347.331	100
C_2H	174.728	165	CH_3C_2H	239.234	72	CH_3C_2H	290.497	106	$HN^{13}C$	348.34	130
C_2H	174.733	103	CH_3C_2H	239.248	121	CH_3C_2H	290.502	125	H_2CS	348.532	50
C_2H	174.807	90	CH_3C_2H	239.252	143	H_2CO	290.623	449	C_2H	349.337	934
Hα	174.996	63	CH_3OH	239.746	119	HC_3N	291.068	22	C_2H	349.339	751
Heα	175.067	20	Hβ	240.021	43	$C^{33}S$	291.486	45	C_2H	349.399	737
HNCO	175.189	24	H_2CS	240.266	27	OCS	291.84	34	C_2H	349.4	553
HNCO	175.189	18	HNCO	240.876	29	HC_3N,v7=1	292.199	29	CH_3CN	349.427	19
HNCO	175.189	21	HNCO	240.876	26	CH_3OH	292.673	144	CH_3CN	349.454	40
HNCO	175.844	106	HNCO	240.876	24	CH_3OH	293.464	35	CH_3OH	350.688	255
HNCO	175.844	82	$C^{34}S$	241.016	233	CS	293.912	1674	NO	350.689	373
HNCO	175.844	94	NH_2CN	241.479	19	CH_3CN	294.28	32	NO	350.691	274
HNCO	176.472	21	CH_3OH	241.7	133	CH_3CN	294.302	70	NO	350.695	199
HNCO	176.472	24	CH_3OH	241.767	175	SO	296.55	166	NO	350.73	24
HNCO	176.472	18	HNCO	241.774	128	NH_2CN	297.869	20	NO	350.737	24
HCN	177.26	423	HNCO	241.774	116	^{34}SO	298.258	18	CH_3OH	350.905	728
HCN	177.26	557	HNCO	241.774	106	NS	299.7	32	NO	350.963	24
HCN	177.261	1175	CH_3OH	241.791	230	NS	299.701	23	NO	350.99	24
HCN	177.261	1987	CH_3OH	241.833	18	NS	300.099	27	NO	351.044	374
HCN	177.262	29	CH_3OH	241.833	18	HC_3N	300.16	16	NO	351.051	275
HCN	177.263	423	CH_3OH	241.842	40	c-C_3H_2	300.192	52	NO	351.052	199
Hβ	177.723	33	CH_3OH	241.844	20	H_2S	300.506	189	SO_2	351.257	15
HCO^+	178.375	3369	CH_3OH	241.879	94	H_2CO	300.837	567	c-C_3H_2	351.523	64
SO	178.605	144	CH_3OH	241.888	40	SO	301.286	160	HNCO	351.633	45
HOC^+	178.972	108	CH_3OH	241.904	66	HC_3N,v7=1	301.325	31	HNCO	351.633	43
C_3H^+	179.903	25	CH_3OH	241.905	76	CH_3OH	302.37	157	HNCO	351.633	40
CH_2NH	180.627	39	HNCO	242.64	29	CH_3OH	303.367	496	H_2CO	351.769	426
CH_3OH	181.296	23	HNCO	242.64	24	SiO	303.927	154	c-C_3H_2	351.782	20
HNC	181.325	2064	HNCO	242.64	26	OCS	303.993	31	c-C_3H_2	351.966	56
CH_3OH	181.771	15	$C^{33}S$	242.914	47	SO	304.078	269	c-C_3H_2	352.194	59
HC_3N	181.945	226	OCS	243.218	39	CH_3OH	304.208	635	Hα	353.623	110
OCS	182.427	29	CH_3OH	243.916	122	H_2CS	304.306	55	CO^+	353.741	26
C_2S	182.553	15	H_2CS	244.048	52	C_2H_5OH	305.354	15	Heα	353.767	34
CH_3CN	183.949	31	c-C_3H_2	244.222	39	C_2H_5OH	305.434	15	$H_2{}^{13}CO$	353.812	23
CH_2NH	183.957	20	CS	244.936	1886	CH_3OH	305.473	513	CO^+	354.014	37
CH_2NH	183.957	29	CH_2NH	245.126	35	$^{13}CH_3OH$	305.699	17	c-C_3H_2	354.143	22
CH_3CN	183.963	67	HC_3N	245.606	83	CH_2NH	306.172	31	HCN,v2	354.46	149
c-C_3H_2	184.33	61	HC_3N,v7=1	246.561	18	CH_2NH	306.172	47	HCN	354.505	6497
^{13}CS	184.982	54	CH_3OH	247.229	22	HNCO	306.554	18	CH_3NH_2	354.844	24
N_2H^+	186.345	648	NO	250.437	138	HNCO	306.554	17	HC_3N,v7=1	356.072	44
CH_3C_2H	187.961	47	NO	250.441	87	HNCO	306.554	16	HCN,v2	356.256	151
CH_3C_2H	187.979	56	NO	250.449	51	CH_3OH	307.166	453	HCO^+	356.734	7789
CH_3C_2H	187.99	96	NO	250.475	16	H_3O^+	307.192	178	HC_3N,v7=2	356.937	15
CH_3C_2H	187.994	114	NO	250.483	16	Hβ	307.258	52	CH_3NH_2	357.44	24
HC_3N	191.04	209	NO	250.708	16	$^{13}CH_3OH$	307.311	15	C_2H_5OH	357.681	16
Hβ	191.057	35	NO	250.753	16	CH_3C_2H	307.53	48	C_2H_5OH	357.682	16
CH_2NH	191.463	39	NO	250.796	138	CH_3C_2H	307.56	56	HOC^+	357.922	248
CH_2NH	191.463	56	NO	250.816	87	CH_3C_2H	307.577	94	CH_3OH	358.606	280
Hα	191.657	68	NO	250.817	52	CH_3C_2H	307.583	112	CH_3C_2H	358.757	28
Heα	191.735	21	c-C_3H_2	251.314	193	HNCO	307.694	82	CH_3C_2H	358.791	33
CH_3OH	191.811	76	c-C_3H_2	251.509	53	HNCO	307.694	76	CH_3C_2H	358.811	56
CH_2NH	192.212	27	CH_3OH	251.738	23	HNCO	307.694	71	CH_3C_2H	358.818	66
$HOCO^+$	192.435	24	CH_3OH	251.812	33	CH_3NH_2	307.792	32	CH_3OH	361.852	25
$C^{34}S$	192.818	178	SO	251.826	145	H_2CS	308.748	29	NH_2CN	362.143	15
CH_3OH	193.415	87	CH_3OH	251.867	39	HNCO	308.798	18	HNC,v2=1	362.554	45
CH_3OH	193.442	112	CH_3OH	251.891	33	HNCO	308.798	17	HNC	362.63	3526
CH_3OH	193.454	151	CH_3OH	251.896	23	HNCO	308.798	16	H_2CO	362.736	329
CH_3OH	193.488	24	CH_3OH	251.9	39	CH_3OH	309.29	346	CH_3OH	363.74	101
c-C_3H_2	193.489	55	CH_3OH	251.906	31	SO	309.502	16	HNC,v2=1	365.147	45
CH_3OH	193.507	61	CH_3OH	251.917	31	CH_3OH	310.193	213	HC_3N,v7=1	365.195	46
CH_3OH	193.511	24	C_2H_5OH	252.951	18	HC_3N,v7=1	310.451	33	HC_3N,v7=2	365.933	15
CH_3OH	193.511	38	C_2H_5OH	252.952	18	CH_3NH_2	310.528	31	HC_3N,v7=2	366.235	15
CH_3OH	193.511	44	NS	253.57	33	CH_3OH	311.853	233	$H_2{}^{13}CO$	366.27	32
$C^{33}S$	194.337	36	NS	253.971	33	CH_3CN	312.664	28	Hβ	366.653	59
OCS	194.586	32	CH_3OH	254.015	60	CH_3CN	312.688	60	CH_2NH	367.072	28
CH_3OH	195.147	79	CH_2NH	254.685	63	SO_2	313.28	21	CH_2NH	367.072	33
C_2S	195.375	15	CH_2NH	254.685	83	CH_3OH	313.597	29	CH_3NH_2	367.681	17
CS	195.954	1566	HC_3N	254.7	66	H_2CS	313.715	56	CH_3CN	367.834	31

Table D.1. continued.

Formula	ν (GHz)	S (mJy)	Formula	ν (GHz)	S (mJy)	Formula	ν (GHz)	S (mJy)	Formula	ν (GHz)	S (mJy)
HNCO	197.085	24	c-C_3H_2	254.988	45	$^{13}C^{18}O$	314.12	18	H_2S	369.101	460
HNCO	197.085	27	OCS	255.374	38	$^{13}C^{18}O$	314.12	25	H_2S	369.127	32
HNCO	197.085	22	$HC^{18}O^+$	255.48	67	CH_3OH	314.86	139	CH_3SH	369.394	17
HNCO	197.821	110	HC_3N,v7=1	255.689	20	CH_3OH	315.267	119	CH_3NH_2	370.166	51
HNCO	197.821	123	HCS^+	256.028	28	OCS	316.146	28	H_2CS	371.844	40
HNCO	197.821	98	CH_3C_2H	256.293	60	Hα	316.415	101	N_2H^+	372.673	1281

by the LTE model should be consistent with the observed spectra and no big outliers should be present. This may not be the case with previously reported species showing some out of equilibrium transitions reported above.

In this section we present details of the modeling of C_2H_5OH, HOCN and HC_3HO, since most relevant details regarding the newly detected isotopologues are discussed in Sect. 5.4. Figs. D.1, D.2, and D.3 show the fit results to these species where the spectral features are ordered by the brightness of the LTE modeled emission, thus showing only the brightest spectral features of each molecule.

We do not list the spectroscopic parameters of the detected transitions since these are directly extracted from the catalog entries indicated in the figures and more importantly these species have been previously identified in the Galactic ISM.

C_2H_5OH: All transitions above 3 mJy modeled emission were used to fit the emission of C_2H_5OH, where those falling within the spectral features of significantly brighter transitions were masked, adding up to a total of ∼50 transitions considered. Among its brightest transitions only the transitions at 287.944 GHz ($6_{4,2} - 5_{3,3}$) and 287.917 GHz ($6_{4,3} - 5_{3,2}$) form an clearly unblended spectral feature. Other spectral lines at 252.952, 270.450, and 234.758 GHz, though partially blended, confirm the detection of C_2H_5OH, together with the fainter feature at 243.556 GHz also marginally blended as displayed in Fig. D.1. The identified transitions appear to show a double peak, similar to what is observed for CH_3OH, further supporting this detection.

HOCN: The brightest expected transition of HOCN in the whole frequency coverage of ALCHEMIS ($10_{0,10} - 9_{0,9}$ at 209.732 GHz) is unambiguously detected and just marginally blended. The brightness of all other transitions drop quickly below the detection limit or are blended to other brighter species as shown in Fig. D.2. All spectral features shown in this figure, but for the one at 251.666 GHz were used in the fit.

HC_3HO: The two brighest transitions of HC_3HO ($14_{0,14} - 13_{0,13}$ @ 129.975 GHz and $15_{0,15} - 14_{0,14}$ @ 139.169 GHz) appear unblended in our survey while most other transitions fall close to the noise level of our obsrevations. We conservatively included transitions down to ∼1 mJy in the fit to this species which may have resulted in an understimate of the brightest transitions. A fit performed exclusively with the two brightest transitions would have resulted into a column density 80% higher yielding $N_{HC_3HO} = 10^{14.2} \pm 10^{13.6}$ cm^{-2}.

Appendix E: Extragalactic molecular census

Table E.1. Chronology of extragalactic detections.

Year	Molecule	Reference	Year	Molecule	Reference	Year	Molecule	Reference
1971	OH	1	2003	SO_2	38	2013	C_2	59
1974	H_2CO	2	2003	NO	38	2013	C_3	59
1975	CO	3	2003	NS	38	2013	HCS^+	60
1975	^{13}CO	4	2003	^{34}SO	38	2013	NH_2CHO	60
1977	H_2O	5	2004	HOC^+	39	2013	^{30}SiO	60
1977	HCN	6	2004	NH	40	2014	H_2Cl^+	61
1978	H_2	7	2004	OH^+	41,42	2014	$H_2^{37}Cl^+$	61
1979	NH_3	8	2006	C_2S	43	2014	NH_2	62
1979	HCO^+	9	2006	NH_2CN	44	2014	$H_2^{17}O$	62
1980	CH	10	2006	$HOCO^+$	44	2014	^{13}CN	63
1985	CS	11	2006	c-C_3H	44	2015	ArH^+	64
1986	c-C_3H_2	12	2006	DNC †	44	2015	$^{38}ArH^+$	64
1987	CH^+	13,14	2006	N_2D^+ †	44	2015	HC_5N	65,66,75
1987	CH_3OH	15	2006	CH_2NH	44,45	2015	CH_3SH	67,68
1988	CN	16	2006	$HC^{18}O^+$	44,46	2016	CF^+	69
1988	C_2H	16	2006	$HC^{17}O^+$	46	2017	$^{13}CH^+$	70
1988	HNC	16	2006	$H^{15}NC$	46,75	2017	SH^+	70
1988	HC_3N	16,17	2006	$H_2^{34}S$	46	2017	$^{34}SH^+$	70
1989	HNCO	18,19	2006	H_3^+	47	2018	CH_3OCH_3	71
1989	$C^{34}S$	20	2006	C_4H_2	48	2018	CH_3OCHO	71
1991	$C^{18}O$	21	2006	C_6H_2	48	2019	HCl	72
1991	$C^{17}O$	21	2006	C_6H_6	48	2019	HCl	72
1991	SO	22,23	2008	H_3O^+	49	2020	O_2 †	73
1991	N_2H^+	24	2009	$C^{33}S$	50	2020	l-C_3H^+	68
1991	SiO	24	2009	$^{13}CH_3OH$	51,52,75	2020	C_3N	68
1991	$H^{13}CO^+$	24	2010	HF	53	2020	CH_2CHCN	68
1991	$HN^{13}C$	24	2010	H_2O^+	53,54	2020	H_2CN	68
1991	$H^{13}CN$	24	2010	$^{13}C^{18}O$	55,56	2020	HCOOH	68,75
1991	CH_3CCH	25	2010	C_{60} †	57	2020	ND	74
1991	CH_3CN	25	2011	$H^{13}CCCN$	58	2020	NH_2D	74
1993	^{13}CS	26	2011	$HC^{13}CCN$	58	2020	HDO	74
1995	OCS	27	2011	$HCC^{13}CN$	58	2021	$H_2^{13}CO$	75
1995	HCO	28	2011	$H_2^{18}O$	58	2021	C_2H_5OH	75
1996	DCO^+	29	2011	^{29}SiO	58	2021	^{13}CCH	75
1996	DCN	29	2011	CH_2CO	58,45	2021	$C^{13}CH$	75
1998	LiH †	30,31	2011	SO^+	45	2021	HOCN	75
1999	$HC^{15}N$	32	2011	l-C_3H	45	2021	$CH_3^{13}CCH$	75
1999	H_2S	33	2011	l-C_3H_2	45	2021	$CH_3C^{13}CH$	75
1999	H_2CS	33,34	2011	CH_2CN	45	2021	$^{13}CH_3CCH$	75
1999	C_2H_2	35	2011	C_4H	45	2021	HC_3HO	75
2000	CO^+	36	2011	CH_3NH_2	45	2021	$Si^{17}O$ †	75
2001	HD	37	2011	CH_3CHO	45			

Notes. Year of first detection of each indiviudal molecular species, were first detections of isotopologues are also included. When first detection was tentative, confirmation is also included. (†) Species where only tentative detection have been reported.

References. (1) Weliachew (1971); (2) Gardner & Whiteoak (1974); (3) Rickard et al. (1975); (4) Solomon & de Zafra (1975); (5) Churchwell et al. (1977); (6) Rickard et al. (1977); (7) Thompson et al. (1978); (8) Martin & Ho (1979); (9) Stark & Wolff (1979); (10) Whiteoak et al. (1980); (11) Henkel & Bally (1985); (12) Seaquist & Bell (1986); (13) Magain & Gillet (1987); (14) Falgarone et al. (2017); (15) Henkel et al. (1987); (16) Henkel et al. (1988); (17) Mauersberger et al. (1990); (18) Nguyen-Q-Rieu et al. (1989); (19) Nguyen-Q-Rieu et al. (1991); (20) Mauersberger & Henkel (1989); (21) Sage et al. (1991); (22) Johansson (1991); (23) Petuchowski & Bennett (1992); (24) Mauersberger & Henkel (1991); (25) Mauersberger et al. (1991); (26) Henkel et al. (1993); (27) Mauersberger et al. (1995); (28) Sage & Ziurys (1995); (29) Chin et al. (1996); (30) Combes & Wiklind (1998); (31) Friedel et al. (2011); (32) Chin et al. (1999); (33) Heikkilä et al. (1999); (34) Martín et al. (2005); (35) van Loon et al. (1999); (36) Fuente et al. (2000); (37) Varshalovich et al. (2001); (38) Martín et al. (2003); (39) Usero et al. (2004); (40) González-Alfonso et al. (2004); (41) González-Alfonso et al. (2004); (42) van der Werf et al. (2010); (43) Martín et al. (2006); (44) Martín et al. (2006); (45) Muller et al. (2011); (46) Muller et al. (2006); (47) Geballe et al. (2006); (48) Bernard-Salas et al. (2006); (49) van der Tak et al. (2008); (50) Wang et al. (2009); (51) Martín et al. (2009a); (52) Muller et al. (2021); (53) van der Werf et al. (2010); (54) Weiß et al. (2010); (55) Martín et al. (2010); (56) Martín et al. (2019b); (57) García-Hernández et al. (2010); (58) Martín et al. (2011); (59) Welty et al. (2013); (60) Muller et al. (2013); (61) Muller et al. (2014a); (62) Muller et al. (2014b); (63) Takano et al. (2014); (64) Müller et al. (2015); (65) Aladro et al. (2015); (66) Costagliola et al. (2015); (67) Meier et al. (2015); (68) Tercero et al. (2020); (69) Muller et al. (2016); (70) Muller et al. (2017); (71) Sewiło et al. (2018); (72) Wallström et al. (2019); (73) Wang et al. (2020); (74) Muller et al. (2020); (75) This work.

The continuous growth of new species detected during the last two decades has resulted in various publications reporting up to date listings of the extragalactic molecular census including conference proceedings (Martín 2009; Martín et al. 2011), refereed publications (Martín et al. 2006, 2011; McGuire 2018), as well as online resources such as that hosted at CDMS[6]. Each of these reports have had different formats and criteria depending on the scope of the publication but all aiming to maintain updated information on first molecular extragalactic detections. Despite these available resources, given the legacy value of ALCHEMI for the extragalactic molecular content, and the relevance of isotopologue detections in this work, which are not included in most of the references above, we provide here a detailed and updated extragalactic molecular census.

In this appendix we provide a comprehensive listing of all molecular species and isotopologues detected in the extragalactic ISM according to the chronology of detections (Table E.1) and grouped by the number of atoms in the molecule (Table E.2). Graphical representations of these lists can be found in Sect. 4.4.

Table E.2. Census of extragalactic molecular species and isotopologues detected.

2 atoms	3 atoms	4 atoms	5 atoms	6 atoms	7 atoms	> 7 atoms
ArH^+, $^{38}ArH^+$	C_2H { ^{13}CCH, $C^{13}CH$ }	C_2H_2	C_4H	C_4H_2	CH_2CHCN	C_2H_5OH
C_2	C_2S	C_3N	c-C_3H_2	CH_3CN	CH_3CCH { $^{13}CH_3CCH$, $CH_3^{13}CCH$, $CH_3C^{13}CH$ }	C_6H_2
CF^+	C_3	c-C_3H	l-C_3H_2	CH_3OH, $^{13}CH_3OH$	CH_3CHO	C_6H_6
CH	H_2Cl^+, $H_2^{37}Cl^+$	l-C_3H	CH_2CN	CH_3SH	CH_3NH_2	C_{60} †
CH^+, $^{13}CH^+$	H_2O { $H_2^{18}O$, $H_2^{17}O$, HDO }	l-C_3H^+	CH_2CO	HC_3HO	HC_5N	CH_3OCH_3
CN, ^{13}CN	H_2O^+	H_2CN	CH_2NH	NH_2CHO		
CO { ^{13}CO, $C^{18}O$, $C^{17}O$, $^{13}C^{18}O$ }	H_2S, $H_2^{34}S$	H_2CO, $H_2^{13}CO$	HC_3N { $H^{13}CCCN$, $HC^{13}CCN$, $HCC^{13}CN$ }			CH_3OCHO
CO^+	H_3^+	H_2CS	HCOOH			
CS { ^{13}CS, $C^{34}S$, $C^{33}S$ }	HCN { $H^{13}CN$, $HC^{15}N$, DCN † }	H_3O^+	NH_2CN			
H_2, HD	HCO	HNCO				
HF	HCO^+ { $H^{13}CO^+$, $HC^{18}O^+$, $HC^{17}O^+$, DCO^+ }	HOCN				
LiH †	HCS^+	$HOCO^+$				
NH, ND	HNC { $HN^{13}C$, $H^{15}NC$, DNC }	NH_3, NH_2D				
NO	HOC^+					
NS	N_2H^+, N_2D^+ †					
O_2 †	NH_2					
OH	OCS					
OH^+	SH^+, $^{34}SH^+$					
SiO { ^{29}SiO, ^{30}SiO, $Si^{17}O$ † }	SO_2					
SO, ^{34}SO						
SO^+						

Notes. Species are alphabetically ordered in each column. (†) Sppecies where only tentative detections have been reported. The table is updated from Martín et al. (2011) according to the list of detections in Table E.1, were references for each detection are provided.

[6] https://cdms.astro.uni-koeln.de/classic/molecules

Appendix F: Full spectrum and model

Fig. F.1 presents the full spectrum analyzed in this article (gray histogram) with the best LTE model fit (red line) as well as the labels for each individual transition with flux density above 100 mJy according to the LTE model. Figs. F.2 to F.11 present a zoomed version of Fig. F.1 in 5 GHz windows and labeling transitions down to 2 mJy. We note that despite what was indicated in Table A.1, the spectral window centered at 368.7 GHz could not be imaged with the 12 m data due to the poor atmospheric transmission. Despite the poorer quality of the data, this spectral window is included in Fig. F.11, which actually shows a bright spectral feature due to H_2S. The quality of the data can only be used to confirm the presence of the line but was not included in the fit.

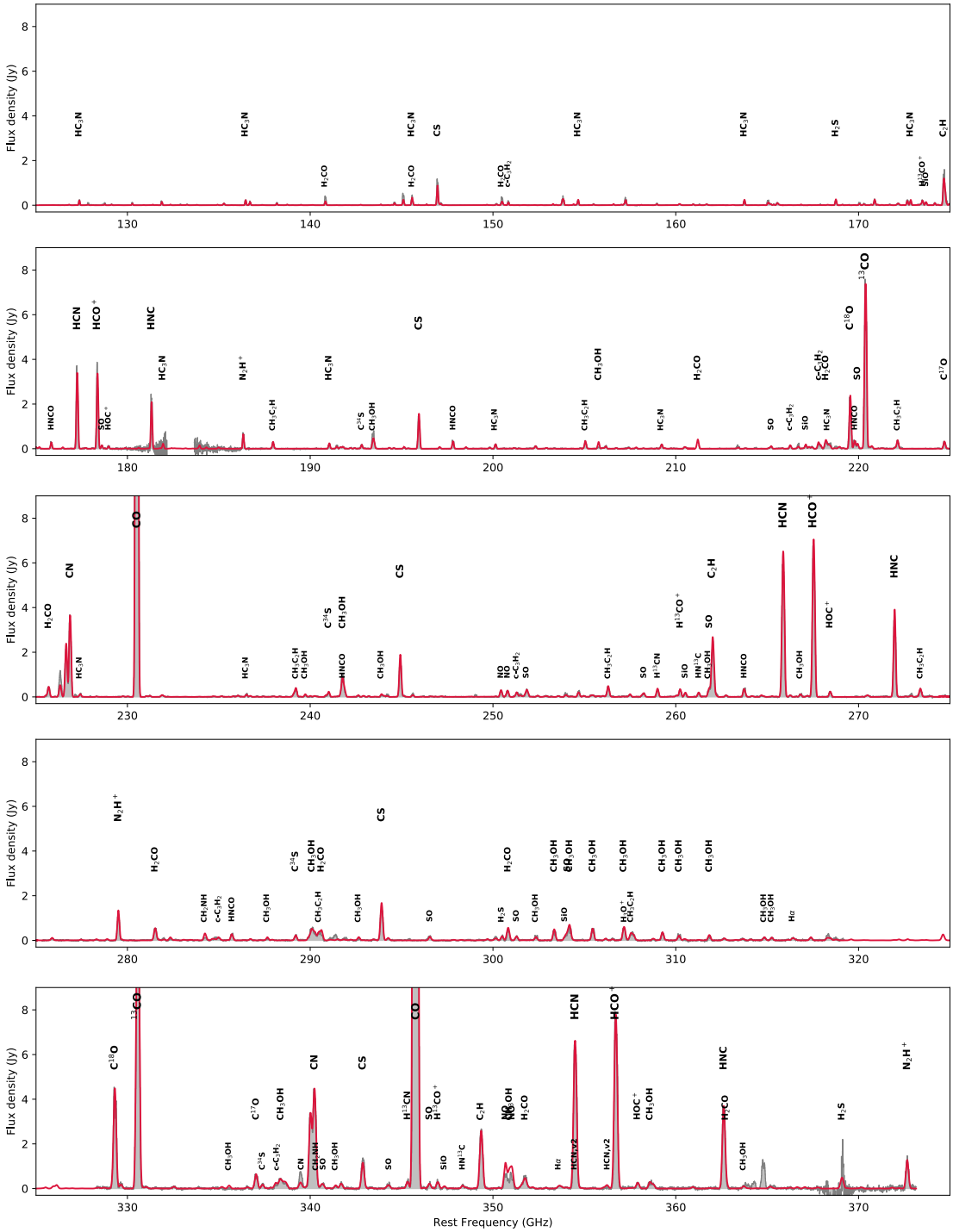

Fig. F.1. Full spectral coverage as in Fig.4 zoomed to 50 GHz frequency windows. The observed spectrum is shown in grey histogram and the model (Sect. 4.3.2) in red line. Only the brighter individual molecular transitions with intensities higher than 100 mJy are labeled with different y-axis position and character size depending on the modelled intensity for > 5, > 1,> 0.2, and > 0.1 Jy.

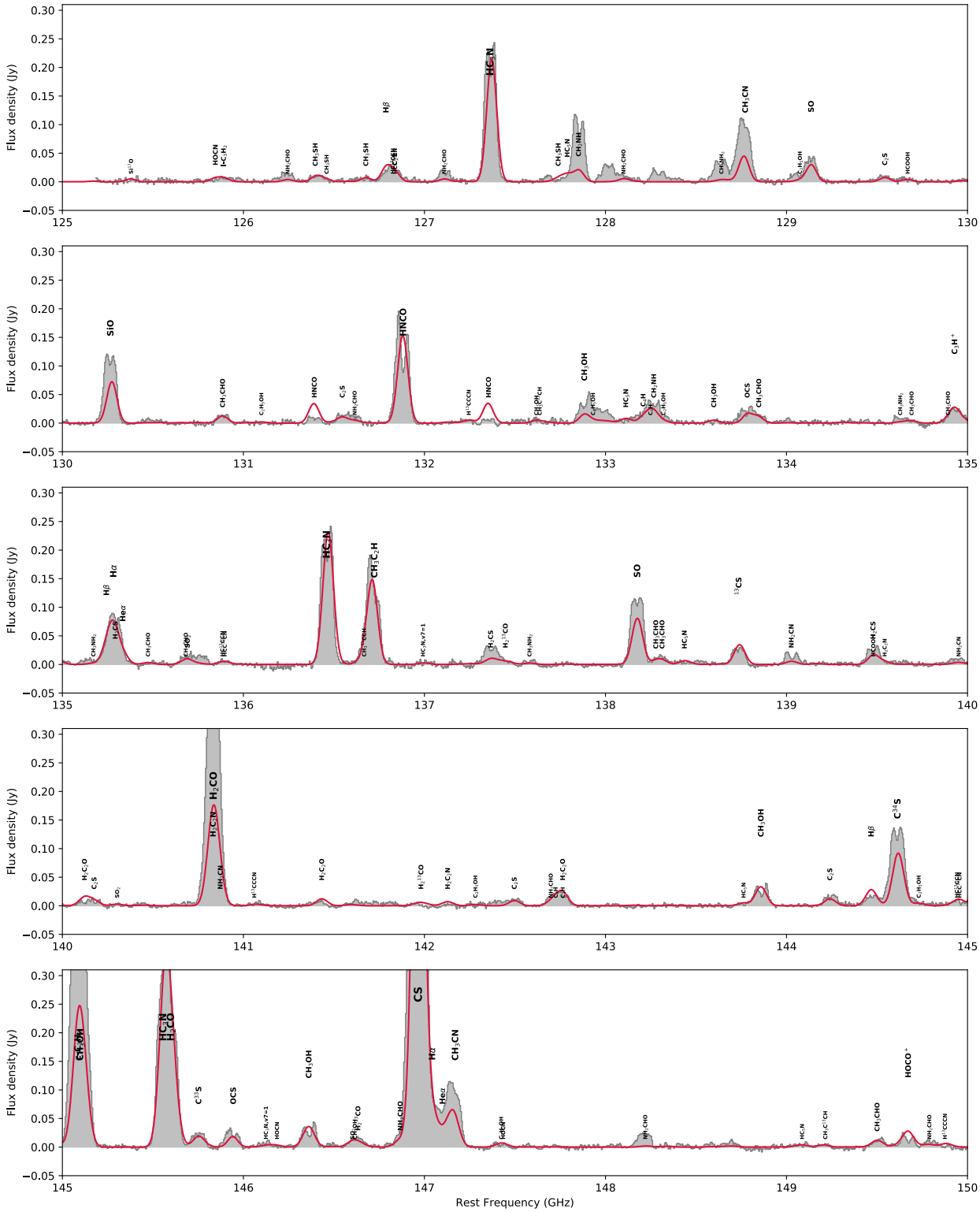

Fig. F.2. Full spectral coverage as in Fig.4 zoomed to 5 GHz frequency windows. The observed spectrum is shown in grey histogram and the model (Sect. 4.3.2) in red line. Individual molecular transitions with intensities higher than 2 mJy are labeled with different y-axis position and character size depending on the modelled intensity for > 270, > 95, > 40, > 20, > 15, > 10, > 5, and > 2 mJy.

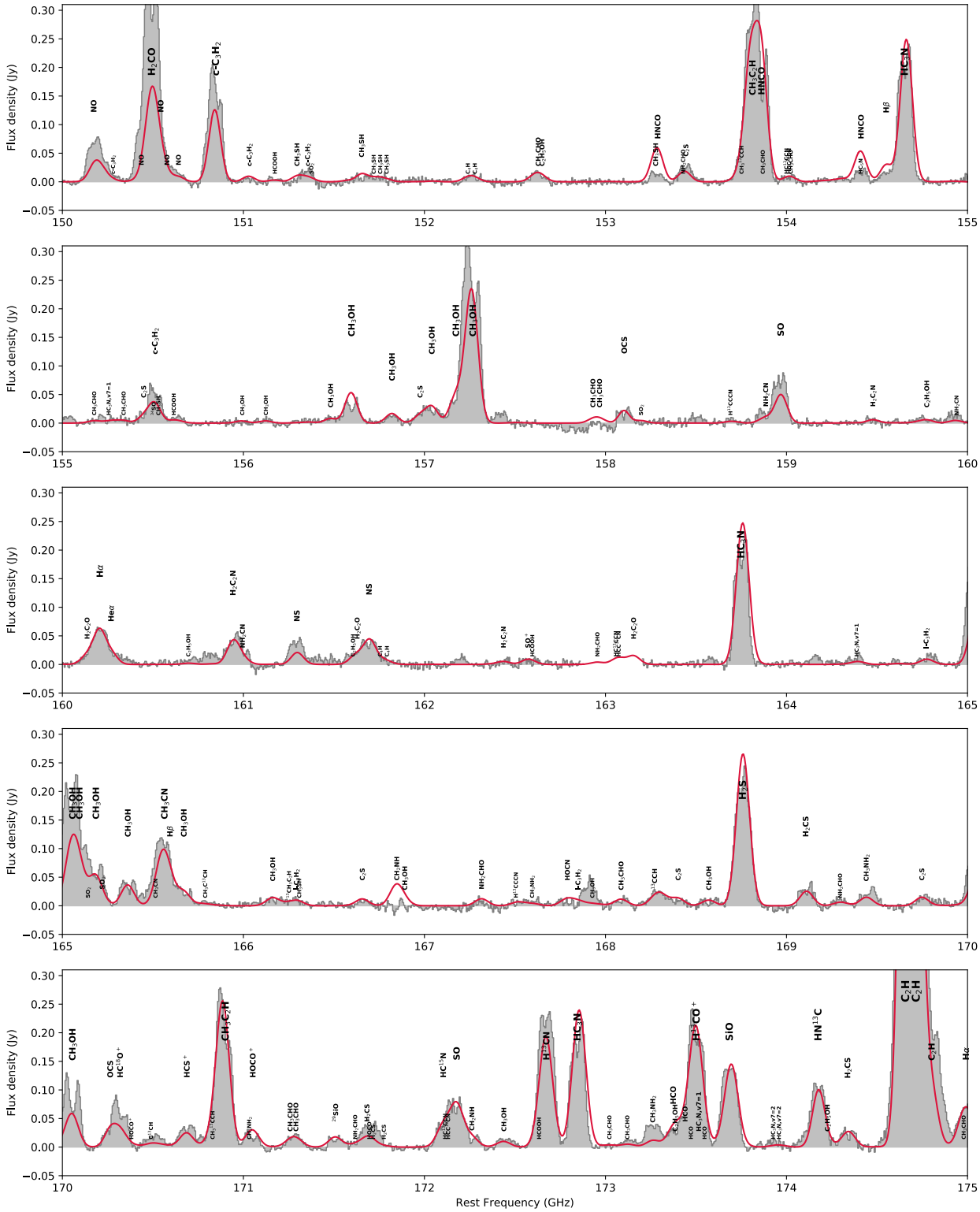

Fig. F.3. Same as Fig. F.2.

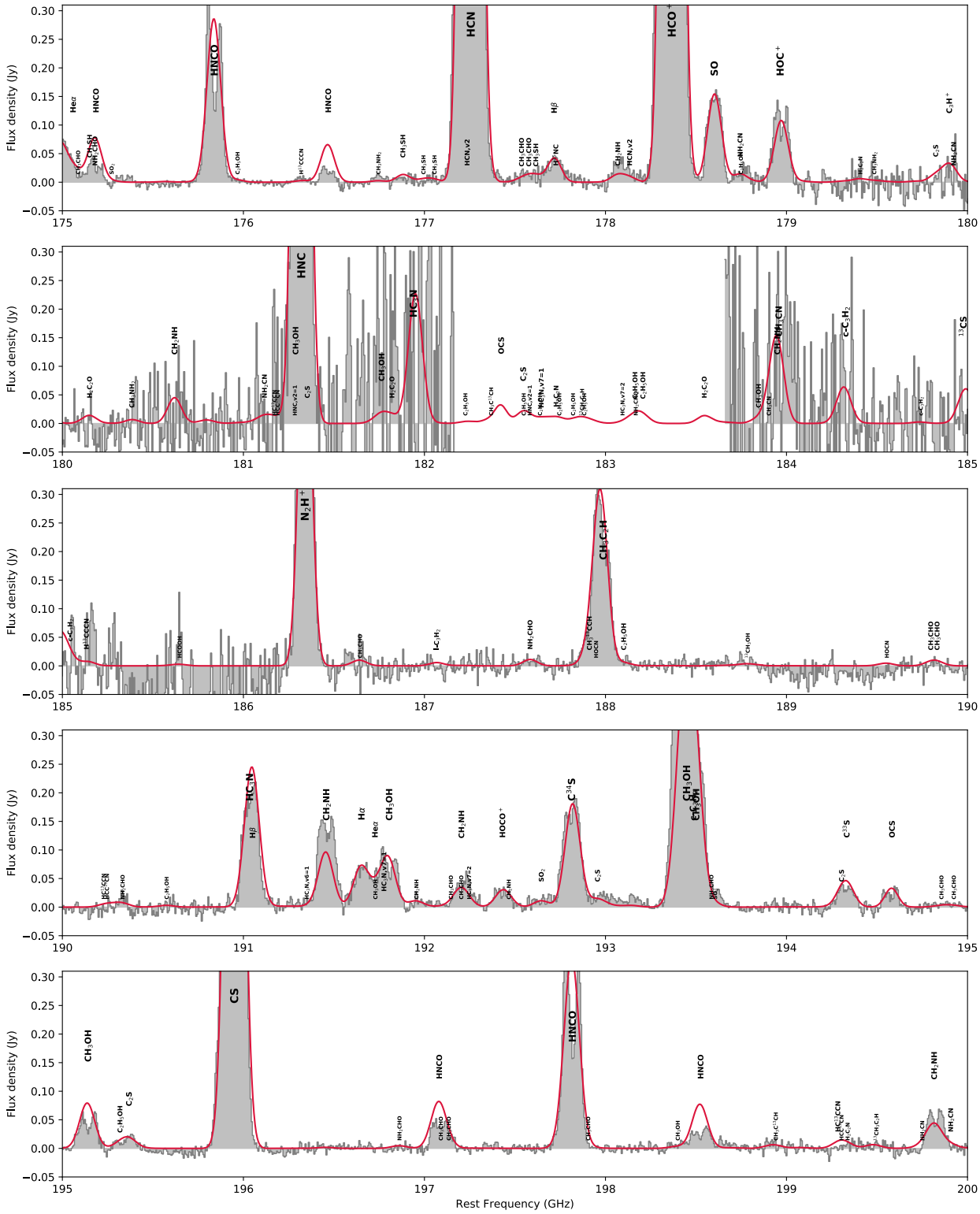

Fig. F.4. Same as Fig. F.2.